

2016

The Production and Manipulation of Nonseparable Spin-Orbit Modes of Light Under Hong-Ou-Mandel Interference Conditions

Maggie E. Lankford

The College of Wooster, mlankford16@wooster.edu

Follow this and additional works at: <http://openworks.wooster.edu/independentstudy>

 Part of the [Optics Commons](#)

Recommended Citation

Lankford, Maggie E., "The Production and Manipulation of Nonseparable Spin-Orbit Modes of Light Under Hong-Ou-Mandel Interference Conditions" (2016). *Senior Independent Study Theses*. Paper 7149.

<http://openworks.wooster.edu/independentstudy/7149>

This Senior Independent Study Thesis Exemplar is brought to you by Open Works, a service of The College of Wooster Libraries. It has been accepted for inclusion in Senior Independent Study Theses by an authorized administrator of Open Works. For more information, please contact openworks@wooster.edu.

The Production and Manipulation of
Nonseparable Spin-Orbit Modes of Light Under
Hong-Ou-Mandel Interference Conditions

Maggie E. Lankford
Physics Department
The College of Wooster

A dissertation submitted in partial fulfillment of the requirements of Senior
Independent Study in Physics at The College of Wooster

Adviser
Dr. Cody Leary

Second Reader
Dr. Susan Lehman

May 6, 2016

Abstract

We report the experimental production of modes of light in which the polarization (spin) and spatial (orbital) degrees of freedom are nonseparable. In addition, the spatial polarization distribution of these modes can be controllably tuned by varying the input polarization state. To achieve this, we input separable spin-orbit modes into an asymmetric Mach-Zehnder interferometer with an extra mirror in one arm. We probed the spatially varying polarization modes by combining a polarization and Stokes-based analysis with CCD imaging. In addition, we predict that two indistinguishable photons entering this device in separable spin-orbit modes can exhibit Hong-Ou-Mandel interference in conjunction with conversion to nonseparable modes. We further measure an additional family of tunable nonseparable modes with spatial polarization distributions, independent of Hong-Ou-Mandel conditions, that can be produced using this interferometer.

Acknowledgments

I would first and foremost like to thank my advisor, Dr. Cody Leary, who has been an invaluable resource in my years at Wooster, and especially in the completion of this project. In addition to being a wonderful mentor and remarkable teacher, he has been incredibly generous with his time, always happy to help me with any difficult problem. It has been his excitement and enthusiasm that has inspired me to see the beauty in the field of optics.

It has been a pleasure working with and learning from the Physics Department at The College of Wooster. Each member of faculty and staff has helped me grow and develop, both as a student and as a human, in often surprising ways. Throughout these four years, I have especially admired Dr. Lehman for being a model woman in physics and an excellent mentor. I would also like to bring to light the contributions of Jackie Middleton, for all her hard work to make the department smooth-running and positive, and Tim Siegenthaler for his mechanical assistance in developing apparatus improvements.

The Clare Boothe Luce Program, funded by the Henry Luce Foundation, was the reason for my initial involvement in the summer of 2014, and I am deeply grateful for this program and the funding that it has given to support this project and my extended involvement with it.

I would next like to thank the Writing Center for all of their assistance, with special thanks to Tessa Hall who had provided both writing assistance and encouragement throughout the entirety of the Independent Study process.

Last but certainly not least I would like to extend my immense gratitude to my family and friends whose love and support seem boundless. To my mother and grandmother, Sylvia and Margaret Hadley, your endless love inspires me to never stop learning and growing, to always look ahead, and to believe in a bright tomorrow.

Much thanks to everyone involved in making this experience both rewarding and fulfilling.

Contents

Abstract	iii
Acknowledgments	v
1 Introduction	1
2 Theory	5
2.1 Light: The traveling wave	5
2.1.1 Hermite Gaussian Modes and the Bloch Sphere	7
2.1.2 The Polarization State	10
2.1.3 Composite traveling wave description	12
2.1.4 A Six-mode Optical Fiber, 2D Sagnac Interferometer, and Optical Rotator: Preparing the Polarization and Spatial State Inputs for Experiment	14
2.1.5 An Asymmetric Mach-Zehnder Interferometer: The Experimental Apparatus	18
2.1.6 One Input	22
2.1.7 Two Identical Inputs	23
2.2 Light as Quanta	26
2.2.1 Developing a Quantum Conversion Factor	27
2.2.2 The Mach-Zehnder interferometer with quantized inputs	28
3 Experiment	31
3.1 Experimental Procedure	31
3.2 HOM Interference Case of Interest	33
3.2.1 Two-input theory	33
3.2.2 One-input Theory	36
3.2.3 Testing the Spatially Varying Polarization Structure	36
3.2.4 Observing Controllable Polarization Structure Changes	38
3.2.5 Investigating a Tunable Spatial Mode	40
3.3 Additional Spatially Varying Polarization Structures	44
4 Conclusions	53
Appendices	
A Derivation of Identical Input Electric Field	55

Bibliography

57

List of Tables

3.1	The results of the experiment designed to create and test nonseparable spin-orbit modes	38
3.2	The comparison of theoretical predictions and experimental data representing an experiment that investigates the role of the parameter β	40
3.3	The theoretical predictions of the input-output relations for the experiment designed to control the output intensity	42
3.4	The intensity distributions of the outputs of the MZI with input parameters $\theta = \phi = \frac{\pi}{2}$, $\beta = 0$	43
3.5	The output of the MZI port d with $\delta = 0$	48
3.6	The theoretical outputs of the MZI for $\theta = \alpha = -\phi = \frac{\pi}{2}$	51
3.7	The comparison between the theory and experiment for the case where $\theta = \alpha = -\phi = \frac{\pi}{2}$	52

List of Figures

2.1	Hermite polynomials $n = 1, 2, 3, 4$ with argument x are shown	8
2.2	A snapshot in time of the oscillating electric field	9
2.3	The intensity of the light in the transverse plane	10
2.4	The Bloch Sphere shown with the axes $x, y,$ and z extended in each direction	11
2.5	The Poincare Sphere shown with the axes $x, y,$ and z extended in each direction	12
2.6	The overall set-up of the experiment including a tracer laser for alignment purposes	13
2.7	A half-wave plate where the birefringent material is oriented with its optical axis tilted at angle θ from the vertical	14
2.8	The 2D Sagnac sorter with the path of the light shown in red	15
2.9	The Sagnac sorts even from odd 2D parity in the manner shown	16
2.10	Like a dove prism, this symmetric configuration of mirrors will rotate a vertical image by 180°	17
2.11	The birefringent crystal inside the Berek compensator shown from above . . .	18
2.12	The asymmetric Mach-Zehnder interferometer	19
3.1	The optical fiber arrangement. The movement of the two black posts	32
3.2	The Gaussian profile tracer laser simplifies the process of precision alignment	33
3.3	The intensity and polarization state of the theoretical inputs, satisfying the conditions	34
3.4	The outputs of the asymmetric MZI, Ψ_{\mp} , for $\theta = \frac{\pi}{2}, \phi = 0,$ and $\alpha = \frac{\pi}{2}$	35
3.5	A schematic of the asymmetric Mach-Zehnder interferometer set-up	37
3.6	An experimental set-up to demonstrate the effect of β on the polarization state of the output modes	39
3.7	The set-up for an experiment where the interferometer output intensities can be controllably varied	41
3.8	The CCD camera interface program that is used to take data	44
3.9	The change in the output polarization structure as β is varied	45
3.10	The set-up for an experiment testing the role of β for a case where $\delta = 0$. . .	47

Chapter 1

Introduction

The nonintuitive discovery that the fundamental building blocks of our universe exhibit both wave and particle natures has generated an increased interest in the field of optics and photonics. This dual nature is often demonstrated through the use of the interference patterns of light in Thomas Young's 1801 double-slit experiment [1].

Historically, physicists believed that light was a wave. While Newton had attempted to prove this theory incorrect, he was unsuccessful in winning over the minds of the majority, and in 1801, Young confirmed in the minds of the physics community, the wave nature of light. The idea of the particle nature of light was not established until 1905 when Einstein published his groundbreaking work, "On a Heuristic Point of View about the Creation and Conversion of Light" [2]. Then, the physics community had to reconcile the idea of particle-wave duality. Since interferometry is a way to investigate light from both particle and wave perspectives, it has been the prevailing method of moving forward the general understanding of the fundamental nature of light itself.

The particle-wave duality paradox becomes important in understanding the concept of interference. Since two superimposed waves are described in a very different way from two "particles", we first must briefly describe the difference in language. When wave physics is used as a tool to understand light, it is called "classical optics" and light is described mathematically as a transverse traveling wave. When light is described as particles, it is called "quantum theory". Incredibly, an interferometer has the power to deal with both scenarios. For this reason, we will follow two related stories: one of the classical theory and one of the quantum.

Classical optics originates from Maxwell's equations. Starting from this fundamental description of an electromagnetic wave, boundary conditions are placed on Maxwell's equations to describe the beam-like geometry of laser light propagating through an interferometric apparatus. The quantum theory of the same apparatus can be developed using Dirac's creation and annihilation operator notation.

Classical light is often used in optical traps, where particles can be captured and manipulated using laser light. Properties of classical light such as polarization and spatial degrees of freedom can impose spin and orbital angular momentum respectively on the trapped particles [3]. The effects of this transfer of angular momentum are used in a range of application, including the study of ultra-cold atoms, condensed matter systems, and biological particles [4, 5]. In this way, classical light is an important tool to probe and control small systems.

Since both polarization and spatial degrees of freedom of light are key to studying these small systems, it is important to understand how they relate to each other. Polarization is simply the direction in which the electric field points as it oscillates, and the spatial state of light is the transverse electric field distribution, or simply a beam cross-section. It is common to represent polarized light as a product mode of these two degrees of freedom, in which the two pieces are independent from each other [6]. In other words, for a given spatial state, the electric field could exhibit any uniform polarization state. Conversely, a given uniform polarization state can be associated with any spatial state.

However, classical optics allows for the “nonseparable” modes in which the polarization is spatially varying, leading to mutual dependence between the spatial and polarization states [7]. Since the analogous quantum properties associated with polarization and spatial degrees of freedom are photon spin and orbital angular momentum, we will call these “nonseparable spin-orbit modes”. We find the nonseparable spin-orbit modes particularly interesting in their application to optical traps and their interaction with cold atoms because developing controlled interplay between spin and orbital angular momentum in an optical trap has great potential.

Since we have noted some application of classical light, it is also important to understand the application of quantum light. The prospect of controllable quantum interference has been a tantalizing prospect for the past few decades, and many experiments are being done around the globe to push the limits of our understanding [8, 9, 10, 11]. An example of an application is using entangled, or correlated, photons to fundamentally secure information transfer over long distances [12]. In this way, creating a quantum internet would allow for the fundamental security needed for financial transactions, or military operations [13, 14].

This exchange of secure information, however, is limited by noise in the signal over distance. In traditional electrical signals, this is solved by using an amplifier, but is not a viable option for quantum information. Instead, photons in conjunction with cold atoms can be used as a “quantum repeater” to clean the quantum signal as it moves over long distances [14, 15]. In this regard, the interaction between photons and cold atoms is fundamental to developing quantum information networks.

These quantum information carriers could also fundamentally change the capabilities of modern computers. Quantum bits can be used in quantum gates, improving speed and increasing the complexity of computations [14]. These three types of applications together: fundamentally secure information, quantum networks, and computing, have the potential to advance the field of information processing in dramatic ways.

We have seen that both classical and quantum interactions with atoms are important in a variety of ways. Here we will investigate one specific type of quantum interference discovered in 1987, Hong-Ou-Mandel (HOM) interference, which gives information about the distinguishability of two photons [16]. In this experiment, we call a possible outcome with two photons involved a joint outcome. Each of these outcomes has a probability of occurring, and we can call that probability an amplitude for the joint outcome state. If two joint outcome states are indistinguishable and the amplitudes equal and opposite then HOM interference occurs. In this scenario the probabilities cancel and the joint outcomes will never occur. This interference pattern was first used to measure the path length difference between two coupled photons passing through an interferometer which gives information about the joint two-photon wave packet [16]. Note that for classical interference, the two waves can superpose and interfere directly, whereas in this type of quantum interference, it is the probability amplitudes that interfere.

Previous studies have shown the possibility of an apparatus, an asymmetric Mach-

Zehnder interferometer (MZI) with an extra mirror in one arm, in which controllably variable nonseparable spin-orbit modes are produced in conjunction with HOM interference [17, 18]. We find that each phenomenon by itself has valuable application, opening the door to a wider range of possibilities when the phenomenon occur simultaneously, including but not limited to encoding two pieces of related information onto a single photon.

The goal of this project is twofold: to refine and condense the theoretical predictions from these studies into a compact theoretical model for the asymmetric MZI under HOM conditions, and to demonstrate the conversion from product to nonseparable spin orbit modes using this theory. Both classical and quantum methods are utilized in presenting the theory for the asymmetric MZI, while classical laser light is used to test the conversion from product to nonseparable spin-orbit modes under the determined HOM conditions.

We also explore an additional family of controllable nonseparable spin-orbit modes that can produced using the asymmetric Mach-Zehnder interferometer. These second exploration does not satisfy the HOM conditions, but still has application in optical traps, and produces another manner in which the spatially varying polarization structure can be controlled.

Chapter 2

Theory

2.1 Light: The traveling wave

To begin the mathematical description of classical interference, we must first lay out the basic description of light: a traveling electromagnetic wave. The starting point is Maxwell's Equations, as stated in [6],

$$\begin{aligned}\nabla \cdot \vec{\mathbf{E}} &= \frac{1}{\epsilon_0} \rho, \\ \nabla \cdot \vec{\mathbf{B}} &= 0, \\ \nabla \times \vec{\mathbf{E}} &= -\frac{\partial \vec{\mathbf{B}}}{\partial t}, \\ \nabla \times \vec{\mathbf{B}} &= \mu_0 \vec{\mathbf{J}} + \mu_0 \epsilon_0 \frac{\partial \vec{\mathbf{E}}}{\partial t}.\end{aligned}\tag{2.1}$$

Here, $\vec{\mathbf{E}}$ is the electric field, $\vec{\mathbf{B}}$ is the magnetic field, ϵ_0 is the permittivity of free space, μ_0 is the permeability of free space, ρ is the charge density, and $\vec{\mathbf{J}}$ is the current density [6].

It is understood that an electromagnetic wave consists of two parts: the electric field and the magnetic field, which are mutually perpendicular. It is common to define the entire electromagnetic wave in terms of the electric field since the magnetic field can be derived from their perpendicular nature. This thesis will follow that trend.

We can now impose two conditions to Maxwell's equations: free space and a beam-like geometry. Free space means that there is no current or charge within the region of interest. The beam-like geometry means that there is very little change in the diameter of the transverse field over large propagation distances. The transverse field is the electric field that is perpendicular to the direction of propagation. If the transverse field changes little over long distances, the beam is collimated and the beam width does not change.

From the free space condition, we find that the differential equation for the electric field simplifies to three independent copies of the wave equation

$$\nabla^2 \vec{\mathbf{E}}(x, y, z, t) - \frac{1}{c^2} \partial_t^2 \vec{\mathbf{E}}(x, y, z, t) = 0,\tag{2.2}$$

as demonstrated in Griffiths' work [6].

Now, it is viable to break the electric field into two parts: the transverse function (E_T) which describes the electric field in the transverse plane, and the longitudinal function (E_L)

which describes the electric field in the longitudinal plane. The total description of the electric field is the product of these two functions

$$\vec{\mathbf{E}}(x, y, z, t) = E_T(x, y, z)E_L(z, t)\hat{\mathbf{e}}, \quad (2.3)$$

with polarization $\hat{\mathbf{e}}$ [19].

It is established that a monochromatic electric field is a wave through time and space that has some angular frequency ω and some wavenumber k and we will call the direction of propagation $\hat{\mathbf{z}}$. The wavenumber is defined to be $2\pi/\lambda$ where λ is the wavelength. In order to keep generality, we must also introduce the longitudinal envelope function, $F(z, t)$, which allows for other changes in the longitudinal plane over time. Given this information, we can write the longitudinal electric field function as

$$E_L(z, t) = F(z, t)e^{i(kz - \omega t)}. \quad (2.4)$$

Substituting Eqns. 2.3 and 2.4 into Maxwell's electric field equation, 2.2, we find the exact free space electric field differential equation

$$[\nabla_T^2 + 2ik(\partial_z + \frac{1}{c}\partial_t) + (\partial_z^2 - \frac{1}{c^2}\partial_t^2)] E_T(x, y, z)F(z, t) = 0, \quad (2.5)$$

where ∇_T^2 is the gradient of the transverse coordinates only (x, y) , and we use the free-space condition of $\omega = kc$.

There is not an exact solution to this differential equation, so assuming the geometry of the system can be used to simplify Eqn. 2.5 into an exactly solvable differential equation.

In this experiment we will be using a Helium Neon laser, which is characterized by high collimation and precise wavelength. Collimated light means that over large distances there is very little change in the width of the beam, giving a beam-like geometry. We can write this relationship as

$$\partial_z^2 E_T(x, y, z) \ll 2k\partial_z E_T(x, y, z), \quad (2.6)$$

where k is the wave number [19, 20]. Using this approximation, Eqn. 2.5 simplifies to the paraxial wave equation

$$\left(\frac{\partial^2}{\partial x^2} + \frac{\partial^2}{\partial y^2} + \frac{\partial^2}{\partial z^2} + 2ik\frac{\partial}{\partial z} \right) E_T(x, y, z) = 0, \quad (2.7)$$

which is exactly solvable.

In the limiting case of a collimated beam, the solution to Eqn. 2.7 is a product of Hermite Polynomials and the Gaussian Function. Again using the beam-like geometry to our advantage, we can solve this differential equation for the case where $z = 0$, since we are interested in the electric field transverse to the propagation direction. This then takes the form

$$E_T(x, y, 0) = \frac{A_{mn}}{w_0} H_m \left(\frac{\sqrt{2}x}{w_0} \right) H_n \left(\frac{\sqrt{2}y}{w_0} \right) e^{-\left(\frac{x^2 + y^2}{w_0^2} \right)}, \quad (2.8)$$

where A_{mn} is a normalization factor of $\sqrt{\frac{2^{-(m+n-1)}}{\pi n! m!}}$, H_n and H_m are the Hermite Polynomials with the argument in parentheses, and w_0 is the beam width parameter [19, 20].

Then inserting Eqns. 2.4 and 2.8 into Eqn. 2.3 the solution to the electric field of a beam propagating in free space is

$$\vec{\mathbf{E}}(x, y, z, t) = \frac{A_{mn}}{w_0} \left[H_m \left(\frac{\sqrt{2}x}{w_0} \right) H_n \left(\frac{\sqrt{2}y}{w_0} \right) e^{-\left(\frac{x^2+y^2}{w_0^2} \right)} \right] e^{i(kz-\omega t)} \hat{\mathbf{e}}. \quad (2.9)$$

We then have a set of orthogonal solutions to the paraxial wave equation that are of the form of traveling waves along the z -axis and are parameterized by the indices m and n [17]. Here let us pause to consider the different components of this electric field equation and determine the intrinsic degrees of freedom of light.

In Eqn. 2.9, the first term, A_{mn}/w_0 , corresponds to an amplitude of the electric field. This will be the function that determines the intensity of the beam when power measurements are taken. The function in square brackets is the transverse spatial mode function which is simply the distribution of the electric field function in a slice perpendicular to the axis of propagation which determines the spatial intensity distribution of the light in the transverse plane. This corresponds to two intrinsic degrees of freedom, one for the x -distribution, one for the y -distribution.

The next piece of the Eqn. 2.9 is the oscillatory part, $e^{i(kz-\omega t)}$. This piece states that the wave propagates along the z -axis with the wave number k and angular frequency ω . Wave number and angular frequency are intimately connected, and together determine the next intrinsic degree of freedom: frequency. This degree of freedom also determines the wavelength of the light since $\omega = 2\pi v/\lambda$ where v is the speed of propagation. In this experiment, the frequency degree of freedom is fixed because we use a Helium Neon laser that has a well-defined, unchanging wavelength at 632.8 nm.

The last piece of the equation is the vector component. The electric field traces out a path in the transverse plane as the electromagnetic wave oscillates. The $\hat{\mathbf{e}}$ component refers to the polarization of the light, which is the last of the four intrinsic degrees of freedom.

2.1.1 Hermite Gaussian Modes and the Bloch Sphere

As shown in the previous section, the transverse spatial mode of the electric field is made up of a product of two Hermite polynomials and a Gaussian function. In Eqn. 2.9 we have written the Hermite Polynomials as

$$H_m \left(\frac{\sqrt{2}x}{w_0} \right), \quad H_n \left(\frac{\sqrt{2}y}{w_0} \right) \quad (2.10)$$

to show that the argument of each function is a constant multiple of x and y respectively.

The Hermite polynomials can be defined as [21]

$$H_n(x) = (-1)^n e^{x^2} \frac{d^n}{dx^n} (e^{-x^2}), \quad (2.11)$$

from which the first three polynomials are found to be

$$\begin{aligned} H_0(x) &= 1, \\ H_1(x) &= 2x, \\ H_2(x) &= 4x^2 - 2. \end{aligned}$$

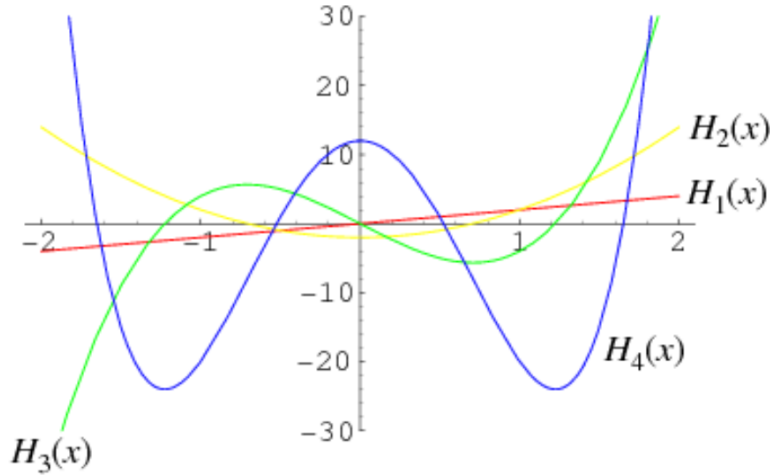


Figure 2.1: Hermite polynomials $n = 1, 2, 3, 4$ with argument x are shown. This graphic was found at [22].

The Hermite functions shown in Eqn. 2.12 are graphed in Fig. 2.1. Here we can see that the order of the function (n) corresponds to the order of the polynomial and consequently the number of roots of the function.

The product of these two Hermite functions, one in x and one in y , with the Gaussian function are called Hermite-Gaussian modes and are ordered based on the value $m + n$. As the order of the mode increases, the number of Hermite Polynomial roots increases, consequently leading to more intricacy in the pattern.

Figure 2.2 shows plots of the scalar amplitude of Eqn. 2.9 where the first three orders of Hermite Gaussian transverse electric field modes are shown as 3D plots. The transverse electric field is plotted against the amplitude of the electric field. These plots are snapshots of the oscillatory electric field in time. The notation for these modes is denoted by HG_{mn} where m and n are the order of the function in x and y respectively.

The intensity of the light is the complex modulus squared of the electric fields [6], denoted

$$I(x, y) = \left| \vec{E}(x, y, z, t) \right|^2 = \vec{E}(x, y, z, t) \cdot \vec{E}^*(x, y, z, t). \quad (2.12)$$

The intensity distribution is what can be measured in the lab with a camera. The intensity of the first three orders of transverse spatial modes are plotted in Fig. 2.3. In these modes, the roots of the Hermite functions appear as vertical or horizontal lines of zero intensity.

Any laser beam can output a superposition of many Hermite Gaussian modes. However, in this experiment we want to focus on the two simplest non-Gaussian transverse spatial modes. These are the two first order Hermite-Gaussian modes shown in Fig. 2.3.

These Hermite Gaussian modes have a radial symmetry, therefore changing to a polar coordinate system will facilitate a concise and clear theory. We can define the coordinates (ρ, Φ) where ρ is the radial coordinate and Φ is the angular coordinate measured from the

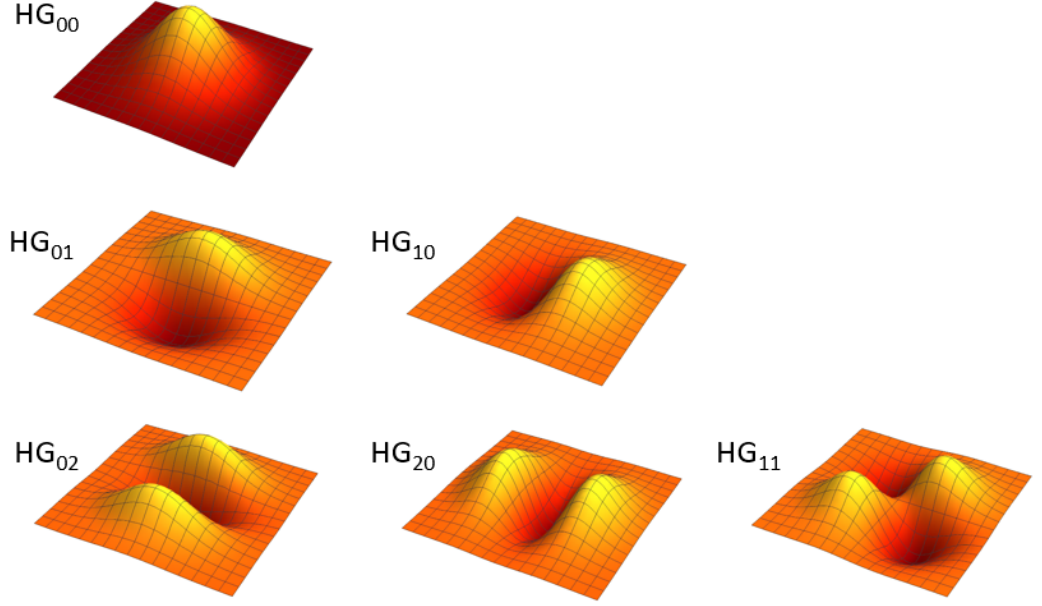


Figure 2.2: A snapshot in time of the oscillating electric field. The x and y coordinates are the transverse spatial coordinates of the electric field and shown by the mesh square, and the third axis shows the amplitude of the field. The top row is zero order Hermite Gaussian modes, the middle row shows the two first order modes, and the bottom row shows the three second order modes. These plots are compiled from a script written by Yashasvi Lohia.

axis $y = 0, x > 0$. Using this coordinate system, the Hermite Gaussian modes can be written as

$$\begin{aligned} HG_{01}(\rho, \Phi) &= \frac{A_{mn}}{w_0} \rho \sin(\Phi) e^{-\left(\frac{\rho}{w_0}\right)^2} \\ HG_{10}(\rho, \Phi) &= \frac{A_{mn}}{w_0} \rho \cos(\Phi) e^{-\left(\frac{\rho}{w_0}\right)^2}. \end{aligned} \quad (2.13)$$

Since we are interested in the first order modes exclusively, we can use a tool called the Bloch Sphere to represent any superposition of these two modes [1]. Here the two basis modes are located at the poles of the sphere. The polar angle θ parameterizes the relative magnitudes of the two basis modes, while the azimuthal angle ϕ parameterizes the relative phase between the basis modes. A Bloch Sphere showing the intensity distributions of the modes along with their coordinates is shown in Fig. 2.4.

Using the Bloch Sphere coordinates, we can write an arbitrary superposition of the two first order Hermite Gaussian modes in Eqn. 2.13 as

$$\begin{aligned} E_T(\theta, \phi; \rho, \Phi) &= \cos\left(\frac{\theta}{2}\right) HG_{01} + \sin\left(\frac{\theta}{2}\right) e^{i\phi} HG_{10} \\ &= \frac{A_{mn}}{w_0} \rho e^{-\left(\frac{\rho}{w_0}\right)^2} \left[\cos\left(\frac{\theta}{2}\right) \sin(\Phi) + e^{i\phi} \sin\left(\frac{\theta}{2}\right) \cos(\Phi) \right]. \end{aligned} \quad (2.14)$$

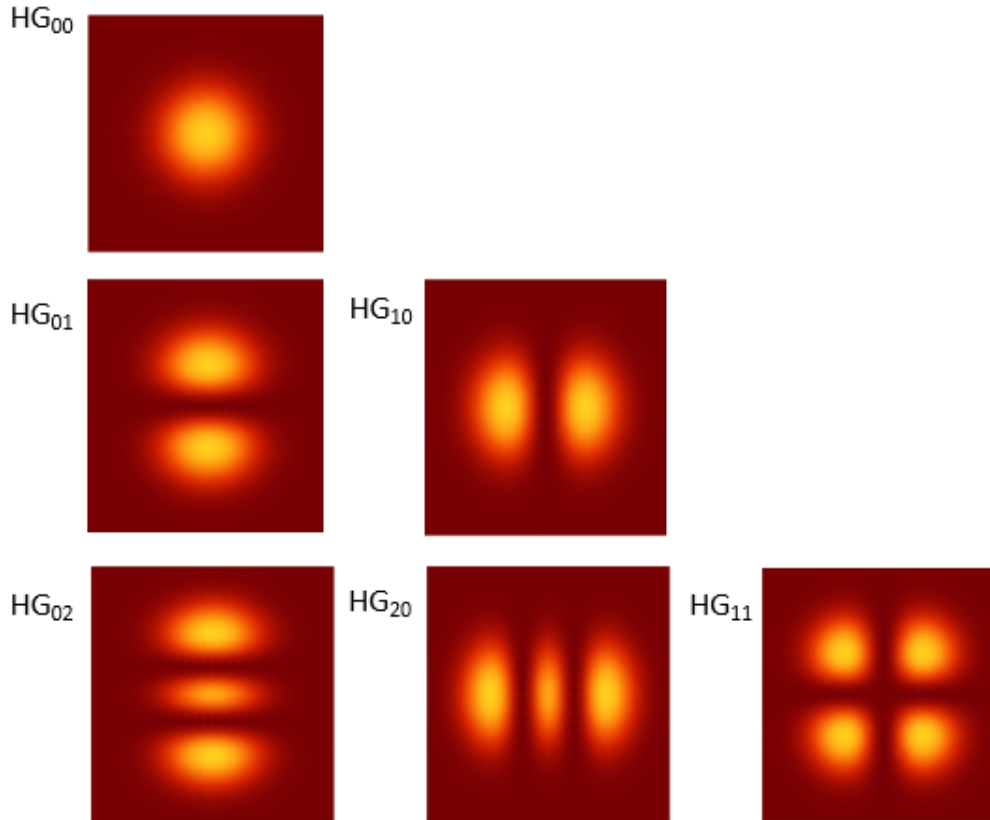


Figure 2.3: The intensity of the light in the transverse plane. The top row is zero order Hermite Gaussian modes, the middle row shows the two first order modes, and the bottom row shows the three second order modes. These plots are compiled from a script written by Yashasvi Lohia.

In the argument of the electric field we separate the ρ , and Φ from the θ , and ϕ because they play different roles. The parameters ρ and Φ show the fundamental dependence of the electric field function, where θ and ϕ simply parameterize the superposition of first order Hermite-Gaussian functions. In this way, we can compactly represent any arbitrary combination of first order Hermite-Gaussian functions, and consequently the transverse spatial state.

2.1.2 The Polarization State

The polarization of the light can also be described using a sphere with two basis vectors. Polarization is usually described as a vector that is an arbitrary superposition of \hat{x} and \hat{y} vectors that can have any phase between them, which can be written as

$$\hat{e} = A\hat{y} + e^{iB}C\hat{x}. \quad (2.15)$$

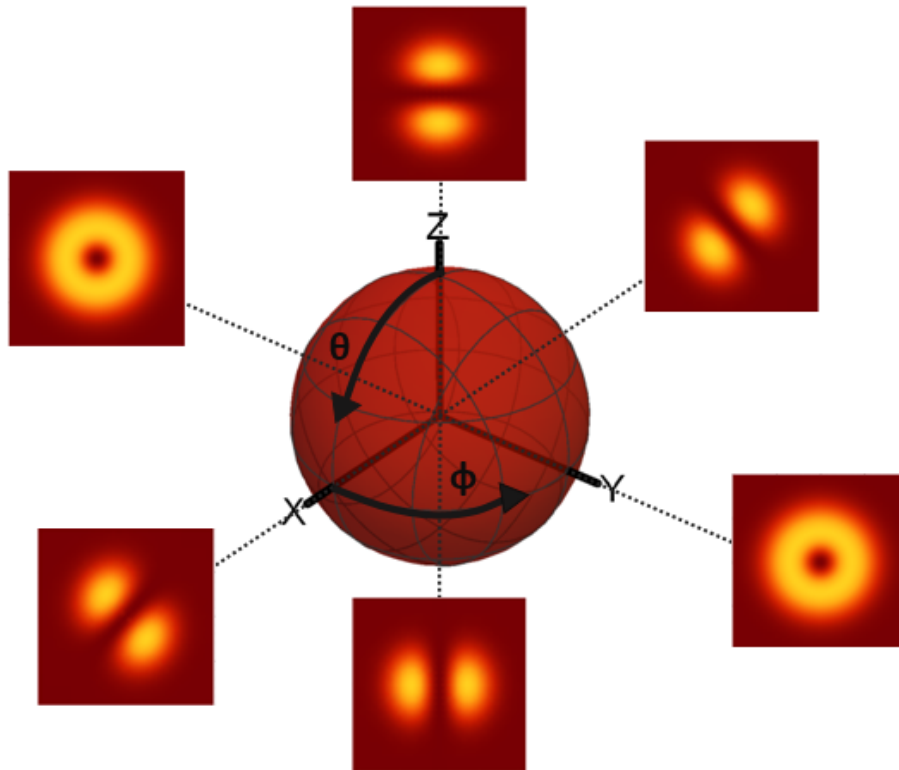


Figure 2.4: The Bloch Sphere shown with the axes x , y , and z extended in each direction. The north and south poles of the sphere represent the two basis modes, each a fundamental first order Hermite Gaussian mode. The polar angle changes the relative magnitude of the two basis modes, and the azimuthal angle shows the phase between them. Each image is shown from the perspective of looking in the propagation direction.

This vector is traditionally written with the relative phase associated with the \hat{y} vector. However, our experimental setup abides by a symmetry associated with the vertical direction. For simplicity, we then use the convention shown above to allow for the symmetries in the mathematics to reflect the symmetries in the lab.

If we use the \hat{x} and \hat{y} polarization as the basis for another sphere in analogy with the Bloch sphere described above, we can use the same theory as with the transverse spatial mode to describe any polarization. This sphere is generally called the Poincaré Sphere and is shown in Fig. 2.5 [1].

Using the Poincaré sphere to describe our arbitrary polarization state, we can rewrite Eqn. 2.15 as

$$\hat{e} = \cos\left(\frac{\alpha}{2}\right)\hat{y} + e^{i\beta}\sin\left(\frac{\alpha}{2}\right)\hat{x}. \quad (2.16)$$

For this sphere, the polar angle is named α and the azimuthal angle β . Analogous to the Bloch Sphere, α parameterizes the relative amplitude of the two basis vectors and β

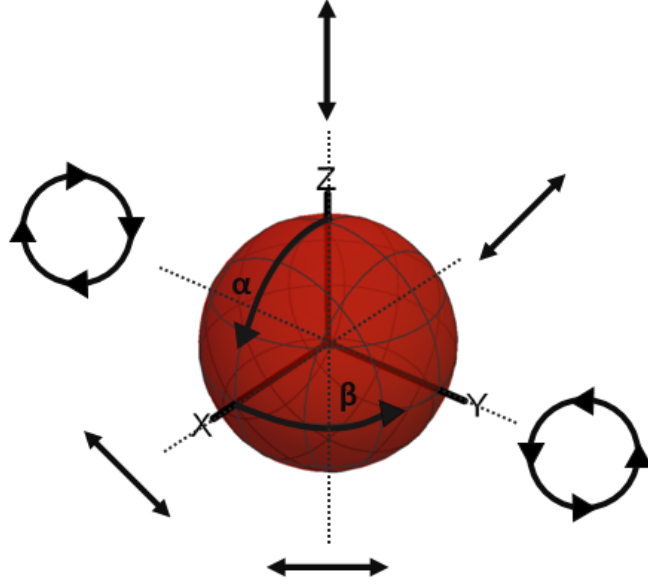


Figure 2.5: The Poincaré Sphere shown with the axes x , y , and z extended in each direction. The north and south poles of the sphere represent the two basis modes, \hat{x} and \hat{y} polarization. The polar angle changes the relative magnitude of the two basis modes, and the azimuthal angle shows the phase between them. Each vector is shown from the perspective of looking in the direction of beam propagation.

parameterizes the relative phase between them. When there is no relative phase between the \hat{x} and \hat{y} vectors, the polarization is linear, but adding a relative phase between the two produces elliptical polarization.

2.1.3 Composite traveling wave description

Now that we have a rigorous definition of the transverse Hermite Gaussian modes, and the polarization, we can write our electric field in its final form,

$$\vec{\mathbf{E}}(\theta, \phi, \alpha, \beta; \rho, \Phi, z, t) = \frac{A_{mn}}{w_0} \rho e^{-\left(\frac{\rho}{w_0}\right)^2} \left[\cos\left(\frac{\theta}{2}\right) \sin(\Phi) + e^{i\phi} \sin\left(\frac{\theta}{2}\right) \cos(\Phi) \right] \\ \times \left[\cos\left(\frac{\alpha}{2}\right) \hat{\mathbf{y}} + e^{i\beta} \sin\left(\frac{\alpha}{2}\right) \hat{\mathbf{x}} \right] e^{i(kz - \omega t)}. \quad (2.17)$$

Since there is a difference between the dependence of the electric field function on the θ, ϕ, α , and β parameters and on the ρ, Φ, z , and t parameters, they are separated by a semicolon. The first set of parameters define the state of the light, meaning any first-order physical beam will have a defined θ, ϕ, α , and β . The second set of parameters describe the fundamental spatio-temporal dependence of the electric field function. When we describe

our physical system with this notation, we will choose the parameters $\theta, \phi, \alpha, \beta$ and describe the electric field only as a function of ρ and Φ , temporarily leaving out the traveling wave piece, since it is understood to always be present.

Equation 2.17 is the complete description of a general superposition of two states of the form Eqn. 2.9; one with $m = 1, n = 0$ the other with $m = 0, n = 1$, and any uniform polarization state. To express a completely general electric field we would need an infinite sum over all Hermite Gaussian functions. To simplify, we are looking only at a small subspace of the functions using only the first order Hermite Gaussian modes.

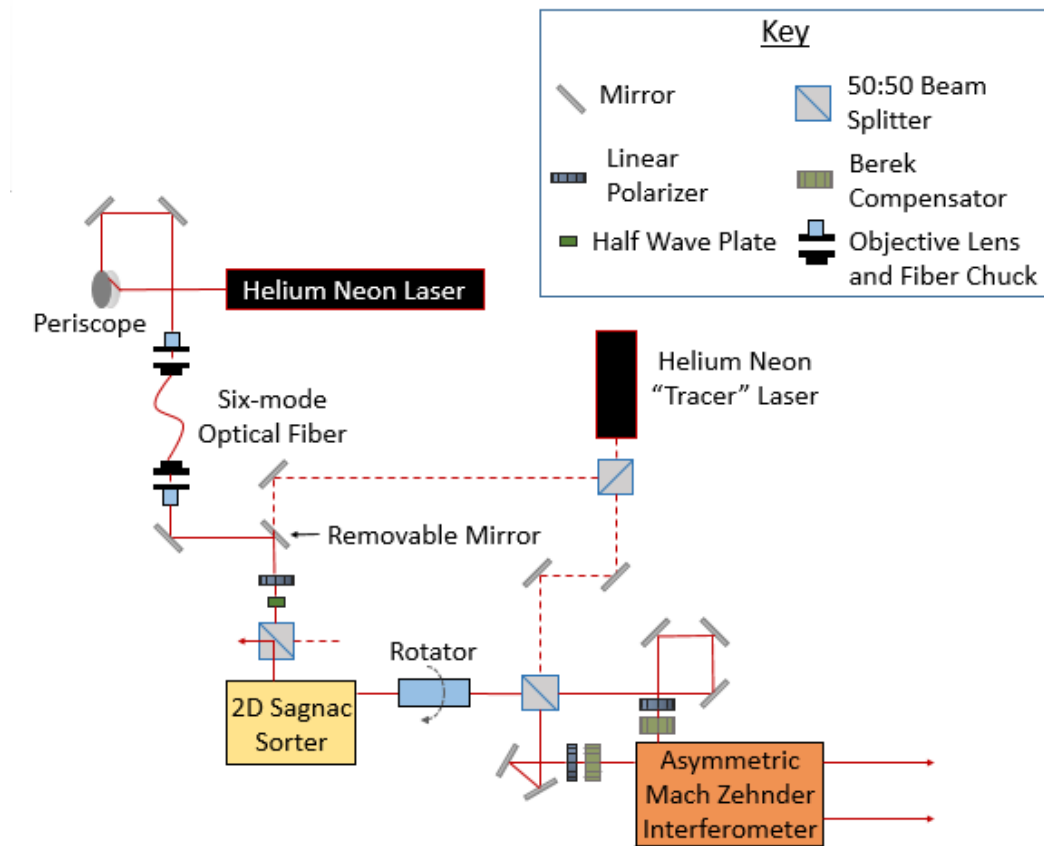


Figure 2.6: The overall set-up of the experiment including a tracer laser for alignment purposes. The direction of propagation of the light is from the upper left corner of the image to the lower right corner, denoted by the solid lines. The tracer laser path is denoted by the dashed lines. The optical fiber, 2D Sagnac sorter and the rotator act as preparation for the main experimental apparatus: the asymmetric Mach-Zehnder interferometer.

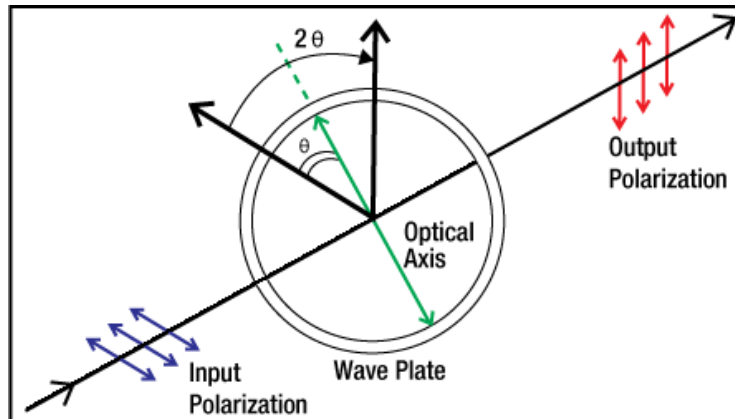


Figure 2.7: A half-wave plate where the birefringent material is oriented with its optical axis tilted at angle θ from the vertical. This has the intended effect of rotating linearly polarized light through angle 2θ . This image is from [23].

2.1.4 A Six-mode Optical Fiber, 2D Sagnac Interferometer, and Optical Rotator: Preparing the Polarization and Spatial State Inputs for Experiment

We are specifically interested in employing an asymmetric Mach-Zehnder interferometer (MZI) in this experiment. This type of interferometer is characterized by two beam-splitters and separate paths between them. In this interferometer, a collimated beam of light is split using the first beam splitter, and the two beams travel independent paths consisting of a differing number of mirrors until they interfere together at the second beam-splitter. This will be used to study mode transformations from product modes to nonseparable spin-orbit modes simultaneously with HOM interference.

In order to prepare the desired inputs of the MZI, we use an optical fiber, a 2D Sagnac sorter, and an optical rotator. The optical fiber excites the first six Hermite Gaussian modes as the light propagates through it, the 2D Sagnac sorter selects the first order Hermite-Gaussian modes and the rotator rotates these modes. This allows us the freedom to select a specific mode to input into the MZI. The entire experimental set-up is shown in Fig. 2.6, and we will briefly discuss the theory of the classical light as it passes through each component. The point of our extensive set-up is twofold: we want to first prepare the light so that we have a linear combination of HG_{01} and HG_{10} modes, then we want to study the interference of these modes in an asymmetric Mach-Zehnder interferometer.

Another interesting aspect of the study of these modes in the asymmetric interferometer is the transformation from polarization and spatial state product mode to nonseparable spin-orbit states. If the amplitudes of the components of polarization and spatial modes basis vectors are equal, the resulting MZI output polarization pattern varies spatially as a controllable nonseparable spin-orbit mode. For this reason, we will focus on these “balanced” input states.

Naturally we start our story with the light source, the Helium-Neon laser which produces a collimated beam with wavelength 632.8 nm [24]. The beam produced consists primarily

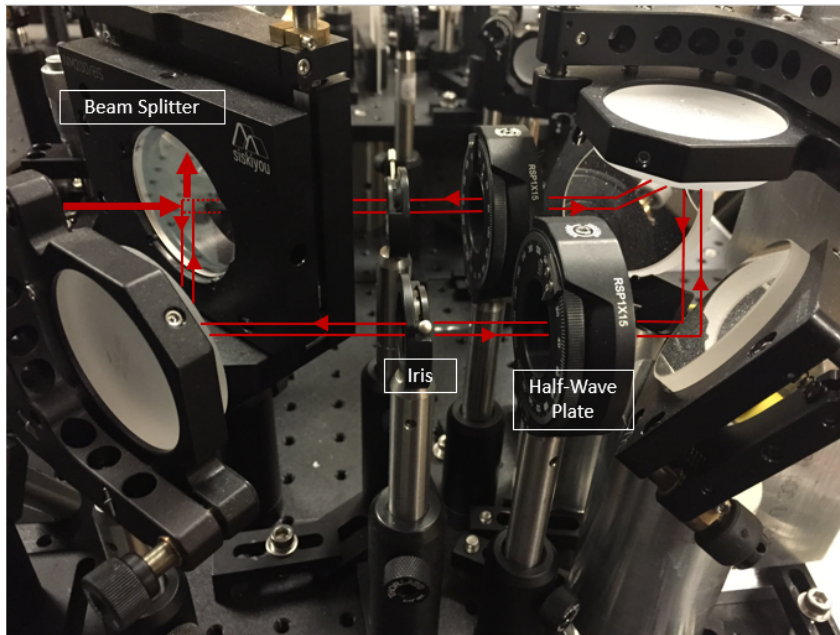


Figure 2.8: The 2D Sagnac sorter with the path of the light shown in red. Note that the path of the light is directed out of the plane to produce the sorting effect. Here the thick lines show the entering and exiting light, while the thin lines show the two directions that the light travels through the device. The displacement of the two paths from each other in the diagram is only for aesthetics. In reality, the two paths need to overlap exactly to produce the 2D sorting effect.

of the Gaussian mode with linear polarization. This is done through a combination of an iris and Brewster angle window on the interior of the laser cavity. The first piece of optical equipment that this laser light encounters is a periscope. This is simply to change the height of the beam propagation above the optical table so that we can have the experiment occur at a different height than the laser.

We then have a microscope objective lens which works to focus the beam down to a smaller width. This allows the beam to enter into the optical fiber. The specific optical fiber used in this experiment is a six-mode fiber at wavelength 632.8 nm, which is used to excite the laser light into higher order spatial modes. Having a six-mode fiber means that there are six different fundamental modes of light that the fiber can excite (HG_{00} , HG_{01} , HG_{10} , HG_{02} , HG_{20} , HG_{11}), which are shown in Fig. 2.3. In reality, each of the six fundamental Hermite-Gaussian modes can have either \hat{x} or \hat{y} polarization, leading to a resulting 12 output modes when polarization is taken into account. This means that the output of the optical fiber is any superposition of these 12 modes.

As discussed in [24], the stresses on the fiber can change its output superposition. By changing the stresses on the fiber, we can have some control about the type of output that we get. Specifically, we want to be able to control the relative phase between the HG_{01} and HG_{10} modes.

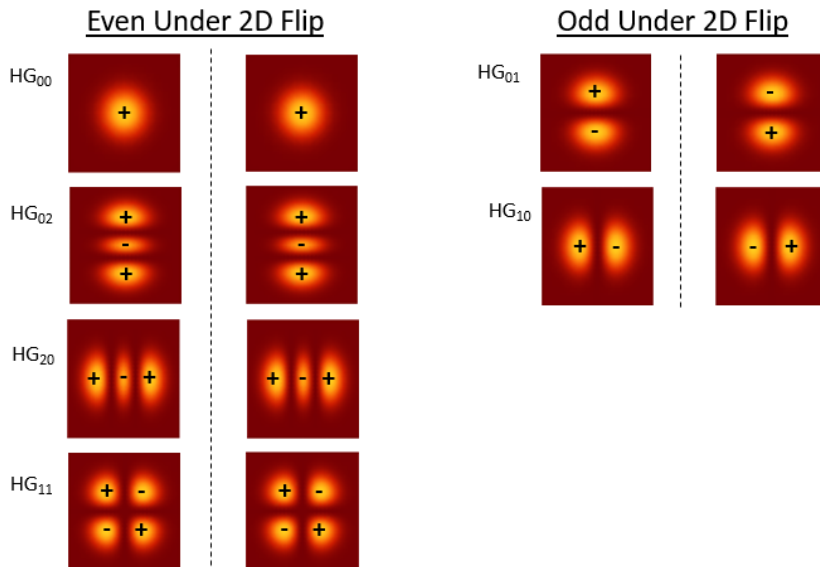


Figure 2.9: The Sagnac sorts even from odd 2D parity in the manner shown. The plus and minus refer to the direction of the electric field in a snapshot of time. As can be seen, the first order Hermite-Gaussian modes are odd under a 2D flip because they are opposite after the operation.

The second microscope objective lens collimates the output of the optical fiber, and the following two mirrors simply redirect the beam. Next the light passes through a linear polarizer and a half-wave plate. These two optical elements together are oriented to produce \hat{y} -polarized light. The point of putting these two elements together is that the polarization of the light out of the fiber can be any superposition of polarization states (including elliptical polarization) and we need the light to be linear and \hat{y} for the 2D Sagnac sorter to work as intended [19]. The polarizer is used to select the major axis of the polarization ellipse, maximizing the intensity while creating linear polarization, and the half-wave plate is used to rotate that linear polarization to \hat{y} .

The theory of the half-wave plate is well-known. It is made of a birefringent material, where the refractive index is dependent on the polarization of light, such that linearly polarized light will rotate through twice the rotation of the birefringent optical axis [25]. This is shown in Fig. 2.7

After the half-wave plate, the light encounters the first 50:50 beam-splitter, which reflects 50% of the light and transmits the other 50%. This is used to view and assess the beam profile before the beam enters into the 2D Sagnac sorter. This sorter is shown in Fig. 2.8, which is characterized by one beam-splitter which splits the light into two parts that travel the same path in opposite directions. The reason we call this interferometer a 2D sorter is because it sorts even from odd parity with respect to a two-dimensional rotation.

To clarify the meaning of this statement, let us briefly discuss these concepts. First, a two dimensional flip is the same effect as a 180° rotation. Here a 2D vector or function centered at the origin is flipped about the x -axis and the y -axis [24]. The parity comments

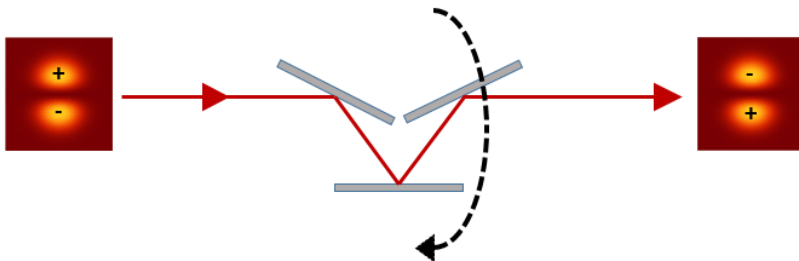


Figure 2.10: Like a dove prism [26], this symmetric configuration of mirrors will rotate a vertical image by 180° . If the whole rotator apparatus is rotated by a degree γ , the image will be rotated by a degree 2γ .

on whether or not the object is the same after the rotation. If the vector or function is unchanged after the two dimensional flip, we call it a positive parity and if the object has changed we say it has negative parity. Although parity can mean many things, we use the term to denote whether or not a vector or function has changed after an operation is performed.

As shown in Fig. 2.9, the two first-order Hermite-Gaussian modes have odd parity with respect to a two-dimensional flip while the rest of the modes exiting the optical fiber have even parity. This means, that the 2D Sagnac sorter effectively isolates out two modes of interest from the rest.

There are two outputs to the Sagnac interferometer. One is in the direction shown: perpendicular to the input. The other travels back against the direction of propagation of the input and encounters again the beam-splitter that sits prior to the 2D Sagnac. Here, the output beam splits so that we can observe the Sagnac even parity output on a screen to get more information about the alignment of the interferometer.

In this way we can use both the output ports to continue to prepare the light that enters into the MZI. The next optical element that is encountered is an optical rotator. This is shown in Fig. 2.10 and consists of three mirrors, two at equal and opposite angles from the third. This configuration of mirrors acts like a Dove prism, rotating the image [26]. We use this device to rotate the modes that are selected by the 2D Sagnac sorter, changing the θ -parameter on the Bloch Sphere. Rotating the apparatus by some angle, γ , will rotate the final image by twice that angle, 2γ .

Next, the light encounters the third beam-splitter, the final stage of preparation for the two inputs of the MZI. As shown in Fig. 2.6, the number of mirrors between this beam-splitter and the MZI differ depending on the path chosen. Each path of the light from the beam-splitter to the MZI encounters three mirror reflections. In this way, the two MZI inputs will be identical unless other optical elements are introduced before the inputs.

Since for each mirror reflection, the \hat{x} and \hat{y} components of the polarization pick up a relative phase between them, we introduce linear polarizers before the MZI inputs to remove this phase, increasing our ability to control the polarization state of the inputs. To carefully control the phase between these vector components we also include a Berek compensator directly before the two inputs of the MZI. The linear polarizer only passes linear light, taking

Plate Angle and Retardation in Berek Compensators

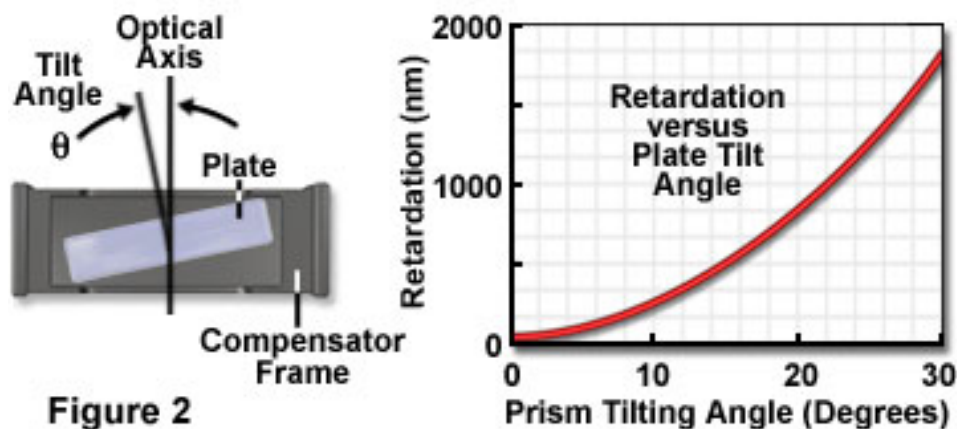


Figure 2.11: The birefringent crystal inside the Berek compensator shown from above where the tilt angle from the optical axis determines the retardation of one polarization component with respect to the other. The right image shows a graph of the retardation versus the crystal tilt angle. Image from [28].

away any elliptical component, while the Berek has the flexibility to rotate the polarization (like the half-wave plate) or to create elliptical or circular polarized light in a controllable manner.

A Berek compensator is made of a birefringent crystal with rotation and tilt degrees of freedom from the beam axis, as shown in Fig. 2.11. The combination of crystal tilt angle and wavelength of light determines the amount by which one polarization component is lagged behind the other. This is called optical retardation, and is determined by the thickness of the crystal in relation to the wavelength [27]. As the tilt angle is varied, the distance that the light will travel through the material changes, so the relationship between the thickness and wavelength changes. The rotation angle allows the slow axis to rotate, changing the polarization component that will be lagged behind the other.

2.1.5 An Asymmetric Mach-Zehnder Interferometer: The Experimental Apparatus

Since the combination of the previously mentioned optical elements allow us to prepare the state of the light as described by Eqn. 2.17, it is now time to delve into the theory of the MZI itself, shown in Fig. 2.12. The first step of this process is to use the tools of linear algebra to model each optical element in the MZI as a matrix. This is helpful because we are using all linear optical tools and we can develop a single matrix to describe the relationship between the inputs and outputs of the MZI.

The interferometer can have two electric field inputs, let's call them a and b , each consisting of a spatial mode component and a polarization component as shown in Eqn. 2.17. Here we can represent either input port as $p = a, b$ and we can re-write Eqn. 2.17 for an

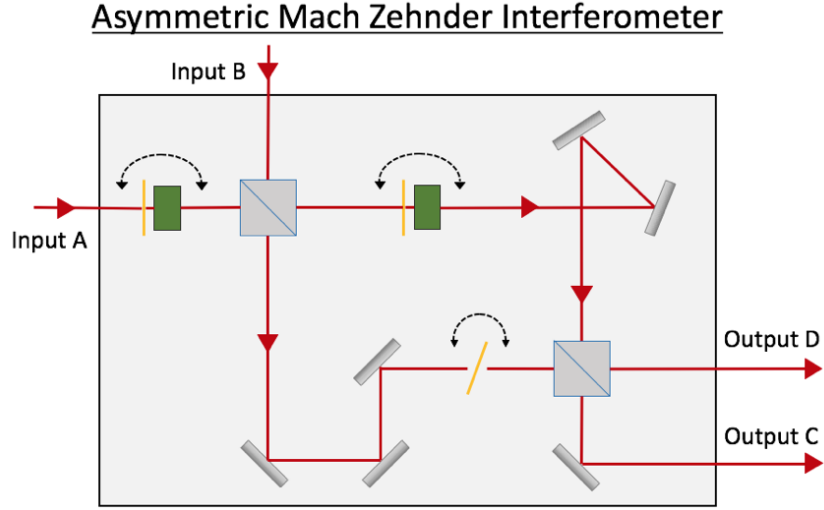


Figure 2.12: The asymmetric Mach-Zehnder interferometer. The key features of this interferometer are the differing number of mirrors in each of the two arms and a phase shifter in the lower arm. It uses the same elements as shown in the key of Fig. 2.6 and an additional yellow phase shifter element. Added to input A and the upper arm of the interferometer are two sets of phase shifter (yellow) and wave-plate (green) combinations. These are simply to compensate for minor phase shifts in the polarization as the light encounters each optical element.

arbitrary product mode input as

$$\vec{\mathbf{E}}_p(\theta_p, \phi_p, \alpha_p, \beta_p; \rho, \Phi, z, t) = S_p(\theta_p, \phi_p; \rho, \Phi) \hat{\mathbf{P}}_p(\alpha_p, \beta_p) e^{i(kz - \omega t)}, \quad (2.18)$$

where S is the spatial function and $\hat{\mathbf{P}}$ is the polarization function. We can call this a product mode because the spatial and polarization components are multiplied together. From this point forward we can neglect the traveling wave parts of Eqns. 2.17 and 2.18 because it is a common piece to all of the electric fields involved. We can then write the spatial function as

$$S(\theta_p, \phi_p; \rho, \Phi) = \frac{N}{w_0} \rho e^{-\left(\frac{\rho}{w_0}\right)^2} \left[\cos\left(\frac{\theta_p}{2}\right) \sin \Phi + e^{i\phi_p} \sin\left(\frac{\theta_p}{2}\right) \cos \Phi \right] \quad (2.19)$$

where N is the normalization factor which includes the factor A_{mn} .

Equation 2.19 can be written in a more compact way if we consider two functions

$$\mathcal{E}_0 \equiv \frac{N}{w_0} \rho e^{-\left(\frac{\rho}{w_0}\right)^2} \sin \Phi \equiv G(\rho) \sin \Phi \quad (2.20)$$

$$\mathcal{E}_1 \equiv \frac{N}{w_0} \rho e^{-\left(\frac{\rho}{w_0}\right)^2} \cos \Phi \equiv G(\rho) \cos \Phi, \quad (2.21)$$

where the normalization factor N is determined such that

$$\int_0^\infty \int_0^\pi \mathcal{E}_0^2 r dr d\Phi = \int_0^\infty \int_0^\pi \mathcal{E}_1^2 r dr d\Phi = 1. \quad (2.22)$$

Using this notation we find that the spatial function in Eqn. 2.19 can be written as

$$S(\theta_p, \phi_p; \rho, \Phi) = A \left[\cos\left(\frac{\theta_p}{2}\right) \mathcal{E}_0 + e^{i\phi_p} \sin\left(\frac{\theta_p}{2}\right) \mathcal{E}_1 \right], \quad (2.23)$$

where A denotes the spatial amplitude.

The polarization can be written as

$$\vec{\mathbf{P}}_p(\alpha_p, \beta_p) = \cos\left(\frac{\alpha_p}{2}\right) \hat{\mathbf{v}}_0 + e^{i\beta_p} \sin\left(\frac{\alpha_p}{2}\right) \hat{\mathbf{v}}_1 \quad (2.24)$$

where $\hat{\mathbf{v}}_0 = \hat{\mathbf{y}}$ and $\hat{\mathbf{v}}_1 = \hat{\mathbf{x}}$ denote the vector components of the polarization.

We can then insert Eqn. 2.23 and 2.24 into Eqn. 2.18 and expand to get the input electric field in the form

$$\vec{\mathbf{E}}_p(\theta_p, \phi_p, \alpha_p, \beta_p; \rho, \Phi) = e_{00}^p \vec{\mathcal{E}}_{00} + e_{11}^p \vec{\mathcal{E}}_{11} + e_{10}^p \vec{\mathcal{E}}_{10} + e_{01}^p \vec{\mathcal{E}}_{01}, \quad (2.25)$$

where

$$\begin{aligned} e_{00}^p &\equiv A \cos\left(\frac{\theta_p}{2}\right) \cos\left(\frac{\alpha_p}{2}\right), & \vec{\mathcal{E}}_{00} &\equiv \mathcal{E}_0 \hat{\mathbf{v}}_0 = G(\rho) \sin(\Phi) \hat{\mathbf{y}}, \\ e_{11}^p &\equiv A \sin\left(\frac{\theta_p}{2}\right) \sin\left(\frac{\alpha_p}{2}\right) e^{i(\phi_p + \beta_p)}, & \vec{\mathcal{E}}_{11} &\equiv \mathcal{E}_1 \hat{\mathbf{v}}_1 = G(\rho) \cos(\Phi) \hat{\mathbf{x}}, \\ e_{01}^p &\equiv A \cos\left(\frac{\theta_p}{2}\right) \sin\left(\frac{\alpha_p}{2}\right) e^{i\beta_p}, & \vec{\mathcal{E}}_{01} &\equiv \mathcal{E}_0 \hat{\mathbf{v}}_1 = G(\rho) \sin(\Phi) \hat{\mathbf{x}}, \\ e_{10}^p &\equiv A \sin\left(\frac{\theta_p}{2}\right) \cos\left(\frac{\alpha_p}{2}\right) e^{i\phi_p}, & \vec{\mathcal{E}}_{10} &\equiv \mathcal{E}_1 \hat{\mathbf{v}}_0 = G(\rho) \cos(\Phi) \hat{\mathbf{y}}. \end{aligned} \quad (2.26)$$

This notation is designed to be consistent with [29], and the following theory is adapted from the same work. Each vector, $\vec{\mathcal{E}}_{jk}$, denotes the vector modes of the electric field, while other pieces of the equation e_{jk}^p denote the complex mode amplitudes where we have replaced each choice of subscript indices 00, 11, 01, and 10 with indices jk where j and k can be zero or one accordingly. The amplitudes of each vector modes are then completely determined with choice of parameter $\theta_p, \phi_p, \alpha_p, \beta_p$, with the total electric field a superposition of these four weighted vector modes.

Each optical element in the MZI can then be represented as a matrix acting on the input vector mode amplitudes e_{jk}^a and e_{jk}^b . The first element of the MZI is a beam-splitter, for which case a new notation of parity must be introduced. While the fundamental idea of parity still applies, in this case we are interested in 1D parity change, or in other words a flip about the y -axis only. We name an operator to describe this parity change, $\hat{\mathbf{\Pi}}$, which acts on the vector modes depending on their parity.

The effect of the $\hat{\mathbf{\Pi}}$ operator acting on the mode $\vec{\mathcal{E}}_{jk}$ is to multiply the mode by either one or negative one such that $\hat{\mathbf{\Pi}} \vec{\mathcal{E}}_{jk} = (-1)^{j+k} \vec{\mathcal{E}}_{jk}$. This operator acts on every reflection of the light through the interferometer.

With this $\hat{\mathbf{\Pi}}$ operator we can adequately describe the actions of both the beam-splitter and the mirrors. The beam-splitter transmits half of the light, and reflects the other half. The reflected light picks up a phase with respect to the transmitted light that in the case of the 50:50 beam-splitter is equal to i [30]. Putting the phase and the mirror reflection together, we obtain a 2×2 matrix representation of a beam-splitter as

$$\hat{\mathbf{U}}_{BS} = \frac{1}{\sqrt{2}} \begin{bmatrix} 1 & i\hat{\mathbf{\Pi}} \\ i\hat{\mathbf{\Pi}} & 1 \end{bmatrix}, \quad (2.27)$$

where $1/\sqrt{2}$ is a normalization factor [30].

The mirror matrix is

$$\hat{\mathbf{U}}_M = \begin{bmatrix} \hat{\mathbf{\Pi}}^n & 0 \\ 0 & \hat{\mathbf{\Pi}}^m \end{bmatrix}, \quad (2.28)$$

because each of the input states is acted on by the $\hat{\mathbf{\Pi}}$ operator. In the mirror matrix, the powers n and m denote the number of mirror reflections in each arm of the interferometer.

Finally, the phase shifter inside the MZI changes the phase of the light in one arm with respect to the other. The matrix representation of this is simply

$$\hat{\mathbf{U}}_\delta = \begin{bmatrix} e^{i\frac{\delta}{2}} & 0 \\ 0 & e^{-i\frac{\delta}{2}} \end{bmatrix}, \quad (2.29)$$

where δ is the phase between the two arms.

Then these three matrices together make the full matrix equation for the MZI,

$$\begin{bmatrix} e_{jk}^c \vec{\mathcal{E}}_{jk} \\ e_{jk}^d \vec{\mathcal{E}}_{jk} \end{bmatrix} = \frac{1}{\sqrt{2}} \begin{bmatrix} 1 & i\hat{\mathbf{\Pi}} \\ i\hat{\mathbf{\Pi}} & 1 \end{bmatrix} \begin{bmatrix} \hat{\mathbf{\Pi}}^2 & 0 \\ 0 & \hat{\mathbf{\Pi}}^3 \end{bmatrix} \\ \times \begin{bmatrix} e^{i\frac{\delta}{2}} & 0 \\ 0 & e^{-i\frac{\delta}{2}} \end{bmatrix} \frac{1}{\sqrt{2}} \begin{bmatrix} 1 & i\hat{\mathbf{\Pi}} \\ i\hat{\mathbf{\Pi}} & 1 \end{bmatrix} \begin{bmatrix} e_{jk}^a \vec{\mathcal{E}}_{jk} \\ e_{jk}^b \vec{\mathcal{E}}_{jk} \end{bmatrix}. \quad (2.30)$$

In our MZI we have two mirrors in one arm and three mirrors in the other, so we can replace variables n and m for the integers two and three. This constitutes a change in the mirror matrix that will impart three mirror reflections for one arm of the MZI and two mirror reflections for the other, which has the same effect as operating with $\hat{\mathbf{\Pi}}$ multiple times.

The next step is to do the matrix multiplication, which results in

$$\begin{bmatrix} e_{jk}^c \vec{\mathcal{E}}_{jk} \\ e_{jk}^d \vec{\mathcal{E}}_{jk} \end{bmatrix} = \frac{1}{2} \begin{bmatrix} e^{i\frac{\delta}{2}} - \hat{\mathbf{\Pi}}e^{-i\frac{\delta}{2}} & i\hat{\mathbf{\Pi}}(e^{i\frac{\delta}{2}} + \hat{\mathbf{\Pi}}e^{-i\frac{\delta}{2}}) \\ i\hat{\mathbf{\Pi}}(e^{i\frac{\delta}{2}} + \hat{\mathbf{\Pi}}e^{-i\frac{\delta}{2}}) & -(e^{i\frac{\delta}{2}} - \hat{\mathbf{\Pi}}e^{-i\frac{\delta}{2}}) \end{bmatrix} \begin{bmatrix} e_{jk}^a \vec{\mathcal{E}}_{jk} \\ e_{jk}^b \vec{\mathcal{E}}_{jk} \end{bmatrix}. \quad (2.31)$$

This matrix shows the relationship between the inputs and outputs of the MZI, which we call $\hat{\mathbf{U}}_{jk}(\hat{\mathbf{\Pi}})$.

There are four options for the subscripts jk , 00, 01, 10, 11, leading to the $\hat{\mathbf{U}}_{jk}(\hat{\mathbf{\Pi}})$ matrix being an 8×8 block diagonal matrix in the expanded form. Instead of writing the expanded matrix in its entirety we can use the $\hat{\mathbf{\Pi}}$ operator to our advantage to write down the two solutions of $\hat{\mathbf{U}}_{jk}(\hat{\mathbf{\Pi}})$.

We know that the $\hat{\mathbf{\Pi}}$ operator works such that $\vec{\mathcal{E}}_{jk} = (-1)^{j+k} \vec{\mathcal{E}}_{jk}$ is true, which allows us to solve for $\hat{\mathbf{U}}_{jk}(\hat{\mathbf{\Pi}})$ when $j+k$ is even and when $j+k$ is odd, leading to

$$\hat{\mathbf{U}}_{\text{even}} = \frac{1}{2} \begin{bmatrix} e^{i\frac{\delta}{2}} - e^{-i\frac{\delta}{2}} & i(e^{i\frac{\delta}{2}} + e^{-i\frac{\delta}{2}}) \\ i(e^{i\frac{\delta}{2}} + e^{-i\frac{\delta}{2}}) & -(e^{i\frac{\delta}{2}} - e^{-i\frac{\delta}{2}}) \end{bmatrix} = i \begin{bmatrix} \sin(\frac{\delta}{2}) & \cos(\frac{\delta}{2}) \\ \cos(\frac{\delta}{2}) & -\sin(\frac{\delta}{2}) \end{bmatrix}, \quad (2.32)$$

when $j+k$ is even and

$$\hat{\mathbf{U}}_{\text{odd}} = \frac{1}{2} \begin{bmatrix} e^{i\frac{\delta}{2}} + e^{-i\frac{\delta}{2}} & -i(e^{i\frac{\delta}{2}} - e^{-i\frac{\delta}{2}}) \\ -i(e^{i\frac{\delta}{2}} - e^{-i\frac{\delta}{2}}) & -(e^{i\frac{\delta}{2}} + e^{-i\frac{\delta}{2}}) \end{bmatrix} = \begin{bmatrix} \cos(\frac{\delta}{2}) & \sin(\frac{\delta}{2}) \\ \sin(\frac{\delta}{2}) & -\cos(\frac{\delta}{2}) \end{bmatrix}, \quad (2.33)$$

when $j + k$ is odd. These matrices together give the full description of our asymmetric Mach-Zehnder interferometer for the range of inputs defined.

2.1.6 One Input

Let's first explore the rich output modes when there is only one input to the asymmetric Mach-Zehnder interferometer. This will not have analogy to the quantum biphoton interference case because biphoton interference involves two photons, however the output modes created can have spatially varying polarization, or nonseparable spin-orbit modes. These types of modes are interesting in their own right. The structure of these states can be mapped onto cold atoms, or used to propagate information, as explored in the introduction.

The only modification that is necessary is to remove input b from Eqn. 2.31 giving

$$\begin{bmatrix} e_{jk}^c \vec{\mathcal{E}}_{jk} \\ e_{jk}^a \vec{\mathcal{E}}_{jk} \end{bmatrix} = \frac{1}{2} \begin{bmatrix} e^{i\frac{\delta}{2}} - \hat{\Pi}e^{-i\frac{\delta}{2}} & i\hat{\Pi} \left(e^{i\frac{\delta}{2}} + \hat{\Pi}e^{-i\frac{\delta}{2}} \right) \\ i\hat{\Pi} \left(e^{i\frac{\delta}{2}} + \hat{\Pi}e^{-i\frac{\delta}{2}} \right) & - \left(e^{i\frac{\delta}{2}} - \hat{\Pi}e^{-i\frac{\delta}{2}} \right) \end{bmatrix} \begin{bmatrix} e_{jk}^a \vec{\mathcal{E}}_{jk} \\ 0 \end{bmatrix}. \quad (2.34)$$

We can then solve this matrix equation four times, once for each combination of indices 00, 11, 01, 10 using Eqns. 2.32 and 2.33, which can still be applied to the new input column vector. After the amplitude of each vector mode is fully determined by the matrix equation, we refer to Eqn. 2.25 to superpose the four vector modes together with their respective amplitudes. The resulting superposition leads to the two output electric fields, written in column vector form for clarity as

$$\begin{bmatrix} \vec{\mathbf{E}}_c \\ \vec{\mathbf{E}}_d \end{bmatrix} = \begin{bmatrix} i \sin\left(\frac{\delta}{2}\right) \left(e_{00}^a \vec{\mathcal{E}}_{00} + e_{11}^a \vec{\mathcal{E}}_{11} \right) + \cos\left(\frac{\delta}{2}\right) \left(e_{01}^a \vec{\mathcal{E}}_{01} + e_{10}^a \vec{\mathcal{E}}_{10} \right) \\ i \cos\left(\frac{\delta}{2}\right) \left(e_{00}^a \vec{\mathcal{E}}_{00} + e_{11}^a \vec{\mathcal{E}}_{11} \right) + \sin\left(\frac{\delta}{2}\right) \left(e_{01}^a \vec{\mathcal{E}}_{01} + e_{10}^a \vec{\mathcal{E}}_{10} \right) \end{bmatrix}. \quad (2.35)$$

This matrix equation can be expanded into two separate electric field equations

$$\begin{aligned} \vec{\mathbf{E}}_c = G(\rho) & \left[i \sin\left(\frac{\delta}{2}\right) \left(\cos\left(\frac{\theta}{2}\right) \cos\left(\frac{\alpha}{2}\right) \sin\Phi \hat{\mathbf{y}} + e^{i(\phi+\beta)} \sin\left(\frac{\theta}{2}\right) \sin\left(\frac{\alpha}{2}\right) \cos\Phi \hat{\mathbf{x}} \right) + \right. \\ & \left. \cos\left(\frac{\delta}{2}\right) \left(e^{i\phi} \left(\sin\left(\frac{\theta}{2}\right) \cos\left(\frac{\alpha}{2}\right) \cos\Phi \hat{\mathbf{y}} + e^{i\beta} \cos\left(\frac{\theta}{2}\right) \sin\left(\frac{\alpha}{2}\right) \sin\Phi \hat{\mathbf{x}} \right) \right) \right], \quad (2.36) \end{aligned}$$

and

$$\begin{aligned} \vec{\mathbf{E}}_d = G(\rho) & \left[i \cos\left(\frac{\delta}{2}\right) \left(\cos\left(\frac{\theta}{2}\right) \cos\left(\frac{\alpha}{2}\right) \sin\Phi \hat{\mathbf{y}} + e^{i(\phi+\beta)} \sin\left(\frac{\theta}{2}\right) \sin\left(\frac{\alpha}{2}\right) \cos\Phi \hat{\mathbf{x}} \right) + \right. \\ & \left. \sin\left(\frac{\delta}{2}\right) \left(e^{i\phi} \sin\left(\frac{\theta}{2}\right) \cos\left(\frac{\alpha}{2}\right) \cos\Phi \hat{\mathbf{y}} + e^{i\beta} \cos\left(\frac{\theta}{2}\right) \sin\left(\frac{\alpha}{2}\right) \sin\Phi \hat{\mathbf{x}} \right) \right]. \quad (2.37) \end{aligned}$$

Note here that the function dependence on δ does not factor out of the spatial and polarization state of the electric field. This means that this parameter has a significant role in both the spatial and polarization mode outputs for the one-input case.

Two special cases to investigate for one-input is when $\delta = \pm\frac{\pi}{2}$. For this case where $\delta = +\frac{\pi}{2}$, Eqn. 2.35 reduces to

$$\begin{bmatrix} \vec{\mathbf{E}}_c \\ \vec{\mathbf{E}}_d \end{bmatrix} = \frac{i}{\sqrt{2}} \begin{bmatrix} \left(e_{00}\vec{\mathcal{E}}_{00} + e_{11}\vec{\mathcal{E}}_{11} \right) - i \left(e_{01}\vec{\mathcal{E}}_{01} + e_{10}\vec{\mathcal{E}}_{10} \right) \\ \left(e_{00}\vec{\mathcal{E}}_{00} + e_{11}\vec{\mathcal{E}}_{11} \right) - i \left(e_{01}\vec{\mathcal{E}}_{01} + e_{10}\vec{\mathcal{E}}_{10} \right) \end{bmatrix}, \quad (2.38)$$

in which case the two outputs are identical. For the case where $\delta = -\frac{\pi}{2}$, Eqn. 2.35 reduces to

$$\begin{bmatrix} \vec{\mathbf{E}}_c \\ \vec{\mathbf{E}}_d \end{bmatrix} = \frac{i}{\sqrt{2}} \begin{bmatrix} - \left(e_{00}^a\vec{\mathcal{E}}_{00} + e_{11}^a\vec{\mathcal{E}}_{11} \right) - i \left(e_{01}^a\vec{\mathcal{E}}_{01} + e_{10}^a\vec{\mathcal{E}}_{10} \right) \\ \left(e_{00}^a\vec{\mathcal{E}}_{00} + e_{11}^a\vec{\mathcal{E}}_{11} \right) + i \left(e_{01}^a\vec{\mathcal{E}}_{01} + e_{10}^a\vec{\mathcal{E}}_{10} \right) \end{bmatrix}, \quad (2.39)$$

in which case the two outputs are identical up to an overall phase factor of -1 , which does not change any measurable quantity.

Here we take the chance to define a useful quantity,

$$\Psi_{\mp}(\theta, \phi, \alpha, \beta; \delta; \rho, \Phi) \equiv \left(e_{00}^a\vec{\mathcal{E}}_{00} + e_{11}^a\vec{\mathcal{E}}_{11} \right) \mp i \left(e_{01}^a\vec{\mathcal{E}}_{01} + e_{10}^a\vec{\mathcal{E}}_{10} \right), \quad (2.40)$$

so that when $\delta = \pm\frac{\pi}{2}$ both output electric fields are identical, up to the factor of negative one, and are Ψ_{\mp} respectively.

2.1.7 Two Identical Inputs

Let's make a simplifying assumption in the spirit of HOM interference, which requires two identical inputs for this interferometer, allowing us to continue forward and investigate a two-input theory. This means $\theta_a = \theta_b \equiv \theta$, $\phi_a = \phi_b \equiv \phi$, $\alpha_a = \alpha_b \equiv \alpha$, and $\beta_a = \beta_b \equiv \beta$ or in other words we have $e_{jk}^a = e_{jk}^b \equiv e_{jk}$.

From Eqns. 2.31-2.33, and using the assumption of identical inputs, we can solve for the amplitudes of the four vector modes in Eqn. 2.25, as we did in the one-input case, and superpose them together to find the complete output electric fields

$$\vec{\mathbf{E}}(\theta, \phi, \alpha, \beta; \delta; \rho, \Phi) = \left(\cos\left(\frac{\delta}{2}\right) \pm \sin\left(\frac{\delta}{2}\right) \right) [\Psi_{\mp}(\theta, \phi, \alpha, \beta; \rho, \Phi)], \quad (2.41)$$

where the choice \mp denotes the choice of output ports c, d respectively and the function Ψ_{\mp} is defined in Eqn. 2.40. Notice here that the overall amplitude of the electric field is dependent on the parameter δ , which has factored out of the function Ψ_{\mp} completely. This parameter, then, will only effect the amplitude of each electric field without effecting the type of mode.

The function $\Psi_{\mp}(\theta, \phi, \alpha, \beta; \rho, \Phi)$ can also be written as

$$\Psi_{\mp}(\theta, \phi, \alpha, \beta; \rho, \Phi) \equiv \cos\left(\frac{\alpha}{2}\right)\tilde{S}_{\mp}\hat{\mathbf{y}} \mp i \sin\left(\frac{\alpha}{2}\right)e^{i\beta}\tilde{S}_{\pm}\hat{\mathbf{x}}, \quad (2.42)$$

where \tilde{S}_{\mp} and \tilde{S}_{\pm} are of the same form as the spatial function modes and are defined to be

$$\begin{aligned} \tilde{S}_{\pm} &\equiv G(\rho) \left[\cos\left(\frac{\theta}{2}\right) \sin \Phi \pm i \sin\left(\frac{\theta}{2}\right) \cos \Phi e^{i\phi} \right], \\ \tilde{S}_{\mp} &\equiv G(\rho) \left[\cos\left(\frac{\theta}{2}\right) \sin \Phi \mp i \sin\left(\frac{\theta}{2}\right) \cos \Phi e^{i\phi} \right]. \end{aligned} \quad (2.43)$$

Equation 2.42 can be expanded using Eqns. 2.43 while still keeping the form $A\hat{\mathbf{y}} + e^{iB}C\hat{\mathbf{x}}$, and inserted into the electric field equation 2.41 to get

$$\vec{\mathbf{E}}(\theta, \phi, \alpha, \beta; \delta; \rho, \Phi) = G(\rho)e^{\left[i \tan^{-1}\left(\frac{M_{\mp}}{R_{\mp}}\right)\right]} \left(\cos\left(\frac{\delta}{2}\right) \pm \sin\left(\frac{\delta}{2}\right)\right) \left[\cos\left(\frac{\alpha}{2}\right)\sqrt{A_{+} \pm B \sin \phi} \hat{\mathbf{y}} \mp i \sin\left(\frac{\alpha}{2}\right)\sqrt{A_{+} \mp B \sin \phi} e^{i\left[\beta \pm \tan^{-1}\left(\frac{B \cos \phi}{A_{-}}\right)\right]} \hat{\mathbf{x}}\right], \quad (2.44)$$

as detailed in Appendix A. Here we have introduced a couple of new functions defined to be

$$\begin{aligned} A_{\pm} &\equiv \cos^2\left(\frac{\theta}{2}\right) \sin^2 \Phi \pm \sin^2\left(\frac{\theta}{2}\right) \cos^2 \Phi \\ B &\equiv \frac{1}{2} \sin \theta \sin(2\Phi) \\ M_{\mp} &\equiv \text{Im}\{\tilde{\mathbf{S}}_{\mp}\} = \mp \sin\left(\frac{\theta}{2}\right) \cos \Phi \cos \phi \\ R_{\mp} &\equiv \text{Re}\{\tilde{\mathbf{S}}_{\mp}\} = \cos\left(\frac{\theta}{2}\right) \sin \Phi \pm \sin\left(\frac{\theta}{2}\right) \cos \Phi \sin \phi. \end{aligned} \quad (2.45)$$

To reiterate, Eqn. 2.44 is the general electric field output of the MZI with identical inputs. Here the amplitude of the electric field for each output port is dependent on the phase shifter δ . Since the phase shifter parameter factors completely out of the modes of the electric field, it has no effect on the electric field other than on amplitude. This means that there is an internal interferometer element that allows us to completely extinguish either output leading to complete constructive interference out one port and complete destructive interference out the other. This is a key element that is important for the quantum HOM interference case given that for quantum inputs we hope to see complete extinction of one output. In this way, the case of $\delta = \pm \frac{\pi}{2}$ where this extinction occurs is a classical case comparable to the quantum HOM interference effect.

There is a nuanced difference between the two-input theory and the single input theory. For the classical two-input complete interference cases, $\delta = \pm \frac{\pi}{2}$ determines the output port at which the light exits the interferometer in addition to determining the output state of the light, Ψ_{\mp} . However, the light exiting port c in will always be in state Ψ_{-} , as determined by Eqn. 2.41 and the light exiting port d in the two-input case will always be in state Ψ_{+} . The internal interferometer parameter, δ , when oriented at other values simply changes the relative magnitude of the electric field out each port.

Another important aspect of Eqn. 2.44 is that there is the phase between the $\hat{\mathbf{x}}$ and $\hat{\mathbf{y}}$ polarization that is dependent on Φ , the azimuthal cylindrical coordinate describing angular location on the transverse spatial mode. This means that there is not necessarily a uniform polarization over the entire mode, but instead one that can vary with transverse mode polar angle. Here we see the appearance of nonseparable spin-orbit modes in which the polarization is spatially varying, the manner in which depends on the input parameters, and will be discussed later for a couple specific cases.

The role of β , the phase between the input vertical and horizontal polarization components, is also a critical concept. This parameter contributes to the output polarization structure, which we have already determines varies with polar angle Φ . As β increases, the phase between the two polarization components at any given polar angle Φ increases. Another way to interpret this is that as β changes, the overall polarization structure rotates about the beam axis. Here we see that the direction of rotation is opposite for choice of \mp .

A nuanced comparison of the single and two-input cases is then that the direction of rotation about the beam axis is the same for each output mode for the single input case,

because the output modes are identical. Here the direction of rotation would be determined by the choice of $\delta = \pm \frac{\pi}{2}$. However, for the two-input case, the mode output is completely determined by the port. For this case, the two output polarization structures would rotate in opposite directions as β is varied.

Since it is directly measurable, another useful piece of information to know is the intensity of light at each output port. In the experiment, we do not measure the electric field directly, we can only see the intensity distribution and measure the power, which is the intensity over a given area. The intensity of the electric field is simply the vector dot product of electric field with its complex conjugate, which results in an expression that is considerably simpler than Eqn. 2.44. The intensity calculation can then be written in multiple steps as

$$\begin{aligned}
 I(\theta, \phi, \alpha, \beta; \delta; \rho, \Phi) &= \vec{E} \cdot \vec{E}^* = E_x E_x^* + E_y E_y^* \\
 &= G(\rho)^2 (1 \pm \sin \delta) [A_+ \pm B \sin \phi \cos \alpha] \\
 &= G(\rho)^2 (1 \pm \sin \delta) [\cos^2(\frac{\theta}{2}) \sin^2 \Phi + \sin^2(\frac{\theta}{2}) \cos^2 \Phi \\
 &\quad \pm \frac{1}{2} \sin \theta \sin(2\Phi) \sin \phi \cos \alpha]. \tag{2.46}
 \end{aligned}$$

The most important piece of information to be gleaned from Eqn. 2.46 is that no matter the input parameters, as long as the inputs are identical, the magnitude of the intensity is governed by the internal phase shifter angle δ . As a reminder, the upper and lower signs denote the output port c , and d respectively. This phenomenon is completely independent of the choice of input parameters, given that they are identical.

The last piece of theory necessary to understand the classical experiment is the theory of a linear polarizer after the output of the MZI. We can understand this using Jones Calculus, which breaks apart the polarization components into a vector with entries \hat{x} and \hat{y} [31]. Like before, we can use a matrix to perform transformations, this time on the Jones polarization vector.

The matrix representation of a linear polarizer is

$$\begin{bmatrix} E_{px}(\Gamma) \\ E_{py}(\Gamma) \end{bmatrix} = \begin{bmatrix} \sin^2 \Gamma & -\sin \Gamma \cos \Gamma \\ -\sin \Gamma \cos \Gamma & \cos^2 \Gamma \end{bmatrix} \begin{bmatrix} E_{px} \\ E_{py} \end{bmatrix}, \tag{2.47}$$

where Γ is measured clockwise from the vertical looking against the direction of propagation [32]. Here E_{px} and E_{py} are the \hat{x} and \hat{y} polarization components of the electric field out port $p = c, d$, and $E_{px,py}(\Gamma)$ are the polarization components after going through the linear polarizer.

Using Eqn. 2.44, we can re-write the Jones vector in Eqn. 2.47 as,

$$\begin{aligned}
 \begin{bmatrix} E_{px}(\Gamma) \\ E_{py}(\Gamma) \end{bmatrix} &= \begin{bmatrix} \sin^2 \Gamma & -\sin \Gamma \cos \Gamma \\ -\sin \Gamma \cos \Gamma & \cos^2 \Gamma \end{bmatrix} \times \\
 &\quad \begin{bmatrix} \mp i \sin(\frac{\alpha}{2}) \sqrt{A_+ \mp B \sin \phi} e^{i \left[\beta \pm \tan^{-1} \left(\frac{B \cos \phi}{A_-} \right) \right]} \\ \cos(\frac{\alpha}{2}) \sqrt{A_+ \pm B \sin \phi} \end{bmatrix}, \tag{2.48}
 \end{aligned}$$

where the overall factor $G(\rho)(\cos(\frac{\delta}{2}) \pm \sin(\frac{\delta}{2})) \exp[i \tan^{-1} \left(\frac{M_{\mp}}{R_{\mp}} \right)]$ has been temporarily left out.

While the electric field after a polarizer is a useful quantity, the measurable piece is the intensity of the light after it passes through the linear polarizer. This is one way that we can

take measurements which reveal information about the polarization pattern of the outputs of the MZI. Since the polarization is spatially varying, the intensity distribution of the light after it passes through the linear polarizer changes based on the angle of the polarizer axis. Therefore the intensity distribution of the light gives information about the polarization pattern of the mode.

To find the intensity of the mode after the linear polarizer, again we find the vector dot product of the electric field through the polarizer with its complex conjugate, leading to

$$I(\Gamma) = \vec{E}_p(\Gamma) \cdot \vec{E}_p^*(\Gamma) = E_{px}(\Gamma)E_{px}^*(\Gamma) + E_{py}(\Gamma)E_{py}^*(\Gamma), \quad (2.49)$$

which expands to

$$I(\Gamma) = G^2(\rho) [1 \pm \sin \delta] \left[\sin^4 \Gamma \sin^2\left(\frac{\alpha}{2}\right)(A_+ \mp B \sin \phi) + \cos^4 \Gamma \cos^2\left(\frac{\alpha}{2}\right)(A_+ \pm B \sin \phi) + \frac{1}{4} \sin^2(2\Gamma)(A_+ \pm B \sin \phi \cos \alpha) \mp \frac{1}{2} \sin \alpha \sin(2\Gamma) \sqrt{A_+^2 - B^2 \sin^2 \phi} \sin\left(\beta \pm \tan^{-1}\left(\frac{B \cos \phi}{A_-}\right)\right) \right]. \quad (2.50)$$

Now we have developed a general theory of the outcome of two identical inputs into the asymmetric MZI, including the electric field equation and the intensity distribution. Because this output polarization can depend on the angle Φ , which is a coordinate describing a radial line on the transverse spatial mode, we introduce a linear polarizer and analyze the intensity distribution. Thus Eqn. 2.50 gives us information about the general case of the intensity distribution using the linear polarizer as a measurement device.

2.2 Light as Quanta

So far, we have restricted the picture of light to a traveling transverse wave. As briefly discussed in the introduction, the outcome of our experiment changes when the inputs are single photons. This is done in practice with a number of methods including single molecules, quantum dots, and spontaneous parametric down conversion [33]. Since we have a comprehensive picture of light as a wave, we can find what occurs when we consider light as a particle. In the classical wave story we found an electric field and intensity function that describes how the waves interfere with each other when going through the asymmetric Mach-Zehnder interferometer. In the quantum story, the particles cannot interfere with each other. Instead we can figure out the probabilities of each possible outcome occurring. We will see that it is possible for the probabilities of different outcomes to cancel with each other, leading to interference of the outcome probability amplitudes. In the classical wave story, the somewhat analogous effect would be complete constructive or destructive interference between fields at the output. We will focus on a specific instance of the interference of probability amplitudes, Hong-Ou-Mandel interference.

2.2.1 Developing a Quantum Conversion Factor

The starting point to translating the classical wave theory into the quantum theory is to quantize Eqn. 2.25, re-written here for convenience,

$$\vec{\mathbf{E}}_p(\theta_p, \phi_p, \alpha_p, \beta_p; \rho, \Phi) = e_{00}^p \vec{\mathbf{E}}_{00} + e_{11}^p \vec{\mathbf{E}}_{11} + e_{10}^p \vec{\mathbf{E}}_{10} + e_{01}^p \vec{\mathbf{E}}_{01}, \quad (2.51)$$

where we can write e_{jk}^p and $\vec{\mathbf{E}}_{jk}$ using the indices j, k to be either zero or one accordingly.

We accept that there is an equality between the total energy of the classical wave and the quantum Hamiltonian operator representing the total energy of a quantum simple harmonic oscillator [30, 34]. The process of quantization uses this principle to form a quantization rule. This rule takes the classical field coefficients as inputs, and outputs a creation or annihilation operator. These operators act on the vacuum state to produce or remove photons with analogous states to the classical light [35].

The two defining qualities of a particle is its energy and its momentum. Einstein showed the relationship $E = hf$ in his discovery of the photoelectric effect, showing that the energy of a photon is proportional to its frequency [2]. The next year, De Broglie found a relationship between momentum and wavelength, $p = h/\lambda$ [36]. Although these two concepts extend beyond photons, it shows, using the relation $c = f\lambda$, that both the energy and momentum are completely determined if either the wavelength or frequency of the light is known. Since this experiment is being restricted to one color of light, we can completely determine the energy of the photons.

We can then look at the total energy of the classical field in a volume. The reason to define this volume is to isolate a finite amount of energy. This volume is defined as a cylinder with infinite cross-sectional area, and finite length L , so that the volume is V_0 .

The total energy of the enclosed wave associated with a given field mode e_{jk} , described in Eqn. 2.26 is then [6, 34]

$$\begin{aligned} H_p &= 2 \epsilon_0 V_0 |e_{jk}^p|^2 \\ &= \epsilon_0 V_0 \left[e_{jk}^p e_{jk}^{p*} + e_{jk}^{p*} e_{jk}^p \right], \end{aligned} \quad (2.52)$$

where ϵ_0 is the permittivity of free space, V_0 is the volume of the cylinder, and $|e_{jk}^p|^2$ is the complex modulus squared of the classical field coefficient.

The quantum Hamiltonian operator representing the total energy of a quantum simple harmonic oscillator is written as [35]

$$\hat{H}_p = \hbar\omega \left[\hat{p}_{jk}^\dagger \hat{p}_{jk} + \frac{1}{2} \right], \quad (2.53)$$

and we can use the commutation relationship [35]

$$\hat{p}_{jk} \hat{p}_{jk}^\dagger = \hat{p}_{jk}^\dagger \hat{p}_{jk} + 1, \quad (2.54)$$

to re-write Eqn. 2.53 as

$$\hat{H}_p = \frac{\hbar\omega}{2} \left[\hat{p}_{jk} \hat{p}_{jk}^\dagger + \hat{p}_{jk}^\dagger \hat{p}_{jk} \right]. \quad (2.55)$$

To better understand the quantization process, we must unpack this compact notation. Each \hat{p} is a quantum operator associated with the port $p = c, d$ of the asymmetric Mach-Zehnder interferometer. The indices are the notation for the field mode of the photon.

The operator with the “dagger” notion, \dagger , designates a creation operator, and the operator without the “dagger” is an annihilation operator. Thus, \hat{p}_{jk}^\dagger creates a photon in the mode associated with the indices (jk) in port p and \hat{p}_{jk} removes a photon in the mode associated with the indices (jk) from port p .

The quantum claim from which all else is derived is that the classical energy in the volume and the quantum Hamiltonian operator representing the total energy of a quantum simple harmonic oscillator are equal [30, 34]. This claim lets us define a quantum conversion factor [34]

$$\begin{aligned} e_{jk}^p &= e_H \hat{p}_{jk} \\ e_{jk}^{p*} &= e_H^* \hat{p}_{jk}^\dagger, \end{aligned} \quad (2.56)$$

where

$$\begin{aligned} e_H &\equiv i \sqrt{\frac{\hbar\omega}{2\epsilon_0 V_0}} \\ e_H^* &\equiv -i \sqrt{\frac{\hbar\omega}{2\epsilon_0 V_0}}. \end{aligned} \quad (2.57)$$

2.2.2 The Mach-Zehnder interferometer with quantized inputs

We can then relate the quantum inputs and outputs of the asymmetric Mach-Zehnder interferometer by performing the quantum conversion Eqn. 2.56 on Eqn. 2.31.

Replacing the classical field coefficients in these equations with the quantum conversion factor, we see that

$$\begin{aligned} \begin{bmatrix} e_H \hat{c}_{jk} \vec{\mathcal{E}}_{jk} \\ e_H \hat{d}_{jk} \vec{\mathcal{E}}_{jk} \end{bmatrix} &= \\ \frac{1}{2} \begin{bmatrix} e^{i\frac{\delta}{2}} - \hat{\Pi} e^{-i\frac{\delta}{2}} & i\hat{\Pi} \left(e^{i\frac{\delta}{2}} + \hat{\Pi} e^{-i\frac{\delta}{2}} \right) \\ i\hat{\Pi} \left(e^{i\frac{\delta}{2}} + \hat{\Pi} e^{-i\frac{\delta}{2}} \right) & - \left(e^{i\frac{\delta}{2}} - \hat{\Pi} e^{-i\frac{\delta}{2}} \right) \end{bmatrix} \begin{bmatrix} e_H \hat{a}_{jk} \vec{\mathcal{E}}_{jk} \\ e_H \hat{b}_{jk} \vec{\mathcal{E}}_{jk} \end{bmatrix}. \end{aligned} \quad (2.58)$$

The $\hat{\Pi}$ operator then acts on the vector modes of light, $\vec{\mathcal{E}}_{jk}$, to give two different matrices: Eqn. 2.32, and Eqn. 2.33. Introducing a new notation for this matrix we can write both matrices in a compact notation as $\hat{\mathbf{U}}_{(\text{even/odd})}$, so that we can refer to both matrices in the same equation.

This new notation allows us to write the quantized asymmetric Mach-Zehnder interferometer as

$$\begin{bmatrix} \hat{c}_{jk} \\ \hat{d}_{jk} \end{bmatrix} = \hat{\mathbf{U}}_{(\text{even/odd})} \begin{bmatrix} \hat{a}_{jk} \\ \hat{b}_{jk} \end{bmatrix}, \quad (2.59)$$

where the quantum conversion coefficient e_H and the vector modes $\vec{\mathcal{E}}_{jk}$ cancel out.

First, it is useful to invert this equation so that we can write inputs on the left and outputs on the right. To do this, we can call upon the fact that for unitary matrices, $\hat{\mathbf{U}}^{-1} = \hat{\mathbf{U}}^\dagger$, where the \dagger notation here means the conjugate transpose of the matrix. Since the Mach-Zehnder interferometer matrix is unitary, we can apply this rule to re-write Eqn. 2.59 as

$$\begin{bmatrix} \hat{a}_{jk} \\ \hat{b}_{jk} \end{bmatrix} = \hat{\mathbf{U}}_{(\text{even/odd})}^\dagger \begin{bmatrix} \hat{c}_{jk} \\ \hat{d}_{jk} \end{bmatrix}. \quad (2.60)$$

The next step is to note that here we have exclusively annihilation operators for the inputs and outputs. However, it will be useful to think in terms of creation operators instead, since in experiment we add photons to the system. To do this, we simply conjugate both sides of the equation to get

$$\begin{bmatrix} \hat{a}_{jk}^\dagger \\ \hat{b}_{jk}^\dagger \end{bmatrix} = \hat{\mathbf{U}}_{(\text{even/odd})}^T \begin{bmatrix} \hat{c}_{jk}^\dagger \\ \hat{d}_{jk}^\dagger \end{bmatrix}, \quad (2.61)$$

where the T means the transpose of the matrix. For these $\hat{\mathbf{U}}_{(\text{even/odd})}$ matrices given in Eqns. 2.32 and 2.33, the transpose is equal to the original matrix.

Since we have determined the relationship between the quantum inputs and outputs of the interferometer, the next step is to write a wave equation for the input and output photons. It is generally accepted that we can superpose the four possible states in each port using photon state amplitudes determined by the Bloch and Poincaré coordinate systems [34]. Since a single photon can be created in state \hat{p}_{jk} when the vacuum is acted upon by the creation operator \hat{p}_{jk}^\dagger , a photon in a superposition of states can be created by a superposition of creation operators acting on the vacuum state. Then we can say that

$$|\psi_{in}\rangle = (e_{00}\hat{a}_{00}^\dagger + e_{11}\hat{a}_{11}^\dagger + e_{10}\hat{a}_{10}^\dagger + e_{01}\hat{a}_{01}^\dagger)(e_{00}\hat{b}_{00}^\dagger + e_{11}\hat{b}_{11}^\dagger + e_{10}\hat{b}_{10}^\dagger + e_{01}\hat{b}_{01}^\dagger) |\text{vac}\rangle, \quad (2.62)$$

represents one photon in port a and one in port b , each in an arbitrary superposition of states \hat{p}_{jk}^\dagger and each acting on the vacuum state. Each operator amplitude is defined as

$$\begin{aligned} e_{00} &\equiv \cos\left(\frac{\theta}{2}\right) \cos\left(\frac{\alpha}{2}\right), \\ e_{11} &\equiv \sin\left(\frac{\theta}{2}\right) \sin\left(\frac{\alpha}{2}\right) e^{i(\phi+\beta)}, \\ e_{01} &\equiv \cos\left(\frac{\theta}{2}\right) \sin\left(\frac{\alpha}{2}\right) e^{i\beta}, \\ e_{10} &\equiv \sin\left(\frac{\theta}{2}\right) \cos\left(\frac{\alpha}{2}\right) e^{i\phi}, \end{aligned}$$

in analogy with classical amplitudes in Eqns. 2.26.

Using the matrix in Eqn. 2.61, we can find the relationship between the interferometer inputs and outputs. Using this relationship, Eqn. 2.62 gives the interferometer output which can be written as [18]

$$\begin{aligned} |\psi_{out}\rangle &= (\hat{\Phi}_c^\dagger + \hat{\Phi}_d^\dagger)(\hat{\chi}_c^\dagger + \hat{\chi}_d^\dagger) |\text{vac}\rangle \\ &= (\hat{\Phi}_c^\dagger \hat{\chi}_c^\dagger - \hat{\Phi}_d^\dagger \hat{\chi}_d^\dagger - \hat{\Phi}_c^\dagger \hat{\chi}_d^\dagger + \hat{\Phi}_d^\dagger \hat{\chi}_c^\dagger) |\text{vac}\rangle, \end{aligned} \quad (2.63)$$

where

$$\begin{aligned} \hat{\Phi}_c^\dagger &\equiv i \left[\sin\left(\frac{\delta}{2}\right)(e_{00}\hat{c}_{00}^\dagger + e_{11}\hat{c}_{11}^\dagger) - i \cos\left(\frac{\delta}{2}\right)(e_{10}\hat{c}_{10}^\dagger + e_{01}\hat{c}_{01}^\dagger) \right], \\ \hat{\chi}_c^\dagger &\equiv i \left[\cos\left(\frac{\delta}{2}\right)(e_{00}\hat{c}_{00}^\dagger + e_{11}\hat{c}_{11}^\dagger) - i \sin\left(\frac{\delta}{2}\right)(e_{10}\hat{c}_{10}^\dagger + e_{01}\hat{c}_{01}^\dagger) \right], \\ \hat{\Phi}_d^\dagger &\equiv i \left[\cos\left(\frac{\delta}{2}\right)(e_{00}\hat{d}_{00}^\dagger + e_{11}\hat{d}_{11}^\dagger) - i \sin\left(\frac{\delta}{2}\right)(e_{10}\hat{d}_{10}^\dagger + e_{01}\hat{d}_{01}^\dagger) \right], \\ \hat{\chi}_d^\dagger &\equiv i \left[\sin\left(\frac{\delta}{2}\right)(e_{00}\hat{d}_{00}^\dagger + e_{11}\hat{d}_{11}^\dagger) - i \cos\left(\frac{\delta}{2}\right)(e_{10}\hat{d}_{10}^\dagger + e_{01}\hat{d}_{01}^\dagger) \right]. \end{aligned} \quad (2.64)$$

Studying Eqn. 2.63, we find that the first term of the four presented in the second line is dependent only on the output port c and the second term is dependent only on the output port d . The last two terms are dependent on both of the output ports. Hong-Ou-Mandel interference occurs when the two photons must exit the same interferometer port together. In other words, Hong-Ou-Mandel interference occurs when $\hat{\Phi}_c^\dagger \hat{\chi}_d^\dagger = \hat{\Phi}_d^\dagger \hat{\chi}_c^\dagger$. Referencing the definitions of these operators, Eqn. 2.64, this equality occurs only when $\delta = \pm \frac{\pi}{2}$ so that the cosine and sine functions are balanced.

Implementing this condition, Eqn. 2.63 is reduced to

$$|\psi_{out}\rangle = (\hat{\Phi}_c^\dagger \hat{\chi}_c^\dagger - \hat{\Phi}_d^\dagger \hat{\chi}_d^\dagger) |\text{vac}\rangle. \quad (2.65)$$

Both operators $\hat{\Phi}_c^\dagger$ and $\hat{\chi}_c^\dagger$ when evaluated at $\delta = \pm \frac{\pi}{2}$ are equal to a factor of ± 1 , and similarly both operators $\hat{\Phi}_d^\dagger$ and $\hat{\chi}_d^\dagger$ are equal to a factor of ± 1 . We can then re-write the product of the two as the square of operators

$$\begin{aligned} \hat{\Phi}_c^\dagger \hat{\chi}_c^\dagger &\equiv \hat{\psi}_c^{\dagger 2} \equiv \left[(e_{00} \hat{c}_{00}^\dagger + e_{11} \hat{c}_{11}^\dagger) \mp i(e_{10} \hat{c}_{10}^\dagger + e_{01} \hat{c}_{01}^\dagger) \right]^2 \\ \hat{\Phi}_d^\dagger \hat{\chi}_d^\dagger &\equiv \hat{\psi}_d^{\dagger 2} \equiv \left[(e_{00} \hat{d}_{00}^\dagger + e_{11} \hat{d}_{11}^\dagger) \mp i(e_{10} \hat{d}_{10}^\dagger + e_{01} \hat{d}_{01}^\dagger) \right]^2, \end{aligned} \quad (2.66)$$

where the square of an operator creates two identical photons in the same port. Here, the choice of \mp denotes a choice of $\delta = \pm \frac{\pi}{2}$, and results in a quantum state analogous to Ψ_\mp implying that the resulting biphoton is in the same nonseparable spin-orbit state as demonstrated in Eqn. 2.41. This is the situation where HOM interference occurs, necessitating identical outputs, and the total output field function can be written as

$$|\psi_{out}\rangle = \mp \frac{1}{2} \left(\hat{\psi}_c^{\dagger 2} - \hat{\psi}_d^{\dagger 2} \right) |\text{vac}\rangle. \quad (2.67)$$

We find that for the quantum two-input case, the output port cannot be predetermined. Instead, the choice of $\delta = \pm \frac{\pi}{2}$ determines the output state of the biphoton as it exits the interferometer. The choice $\delta = +\frac{\pi}{2}$ ensures HOM interference will occur with state Ψ_- , and the choice $\delta = -\frac{\pi}{2}$ ensures HOM interference will occur with state Ψ_+ .

Chapter 3

Experiment

3.1 Experimental Procedure

In Section 2.1.4 we explored each piece of the experimental set-up and its contribution to the preparation of the experimental input modes for the asymmetric Mach-Zehnder interferometer. Here we look at a brief procedure for the mode preparation and Mach-Zehnder alignment.

Using Fig. 2.6 as a guide for the procedure, we start with the preparation of the optical fiber. Here we have interlaced the fiber between a set of three posts, as shown in Fig. 3.1. The outer two posts are on movable stands so that sliding them forwards and backwards adjusts the curvature of the fiber, changing the output mode. Since we have set up the fiber so that it lies about six inches above the optical table, we set up stands on either side of the posts in order to support the fiber. To gain even more control over the curvature in the fiber, vertical height blockers were added so that the vertical movement of the fiber was restricted from both above and below. With this restriction, the vertical pitch of the fiber becomes increasingly important. Using the combination of fiber-bending with the posts and fiber-torsion by changing the pitch, the phase between the two basis first order spatial modes can be manipulated. The combination of the stands and these height blockers also provided a safety to restrict the motion of the fiber were it to slip out of place, decreasing the chance of the fiber coming out of the fiber chuck and mounts.

The next major piece of alignment is the 2D Sagnac Sorter. To make initial alignment easier, a second Helium Neon laser with a Gaussian spatial profile was used as a “tracer” laser. This means that the path of the original laser light is traced out by this new laser, as shown in Fig. 3.2. Using the tracer laser Gaussian beam, the Sagnac could be aligned using power measurements instead of being aligned using spatial intensity distributions as done with higher order modes. Since the Gaussian is even under 180° rotation, all of the light will exit the even port of the Sagnac interferometer. Using a power meter, the intensity out the odd port of the Sagnac can be minimized using techniques detailed in [17], to indicate the best alignment of the interferometer.

The last significant piece of alignment is the asymmetric Mach-Zehnder interferometer. Again, the Gaussian tracer laser was needed for this alignment process. Using the single input of the Gaussian tracer laser, the internal workings of the Mach-Zehnder interferometer could be aligned using the techniques described in [17]. The theoretical predictions of the outputs for this case are given in [37], where varying the glass plate angle δ changes the

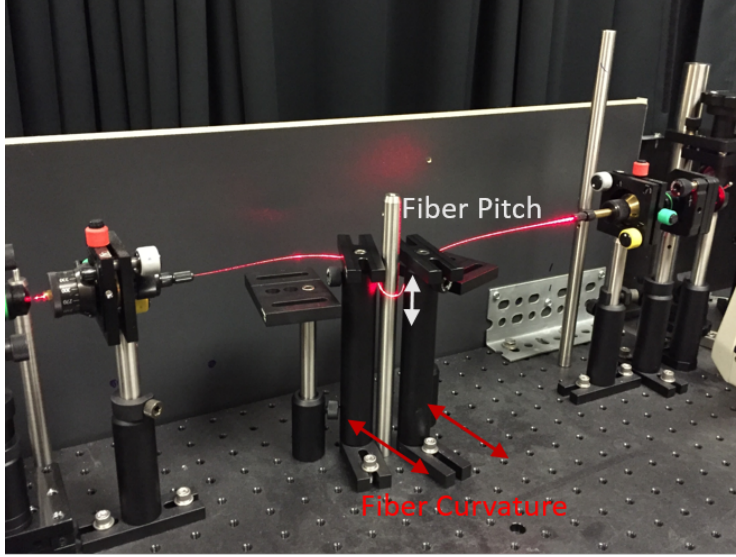


Figure 3.1: The optical fiber arrangement. The movement of the two black posts, shown by the black arrows control the curvature of the fiber, while the position of the fiber around the center post can be changed to manipulate the fiber pitch. The combination of these change the phase between the two first order Hermite Gaussian spatial modes.

relative intensity of the two output ports.

Interferometric visibility is a measure of complete interference and can be written in two ways

$$\text{Visibility} = \frac{I_{c\max} - I_{d\min}}{I_{c\max} + I_{d\min}} = \frac{I_{d\max} - I_{c\min}}{I_{d\max} + I_{c\min}}, \quad (3.1)$$

where $I_{c\max}$, and $I_{d\max}$ are the maximum power out the ports c , and d respectively, and $I_{c\min}$ and $I_{d\min}$ are the minimum power out the two ports.

Since the visibilities defined in these different ways are only equal for ideal systems, an average of the two is used to measure the visibility. Using the technique mentioned above with the tracer laser, the asymmetric Mach-Zehnder interferometer exhibited a visibility of 0.849 when the spatial mode interference was best. In the future, work should be done to model the best expected visibility using imperfect beam splitters.

It is also necessary to understand that each reflective piece in the Mach-Zehnder interferometer is not ideal. Upon each reflection, the \hat{x} and \hat{y} components of the polarization have different phases imparted on them. The phase difference imparted between the two must be corrected in order for the interference to occur as theorized. To fix this, a glass plate and half wave plate was inserted into one arm of the interferometer and tilted to impose a phase difference between the two polarization components, correcting for the imperfections of the reflective surfaces of our apparatus.

Finally, the data collection was taken with a CCD camera, which was protected by a number of neutral density filters that uniformly attenuate the intensity of the outputs. In order to get the best information about the output states, we adjusted the filters so that very few pixels of the camera were saturated. This gives us a better idea of the relative intensities

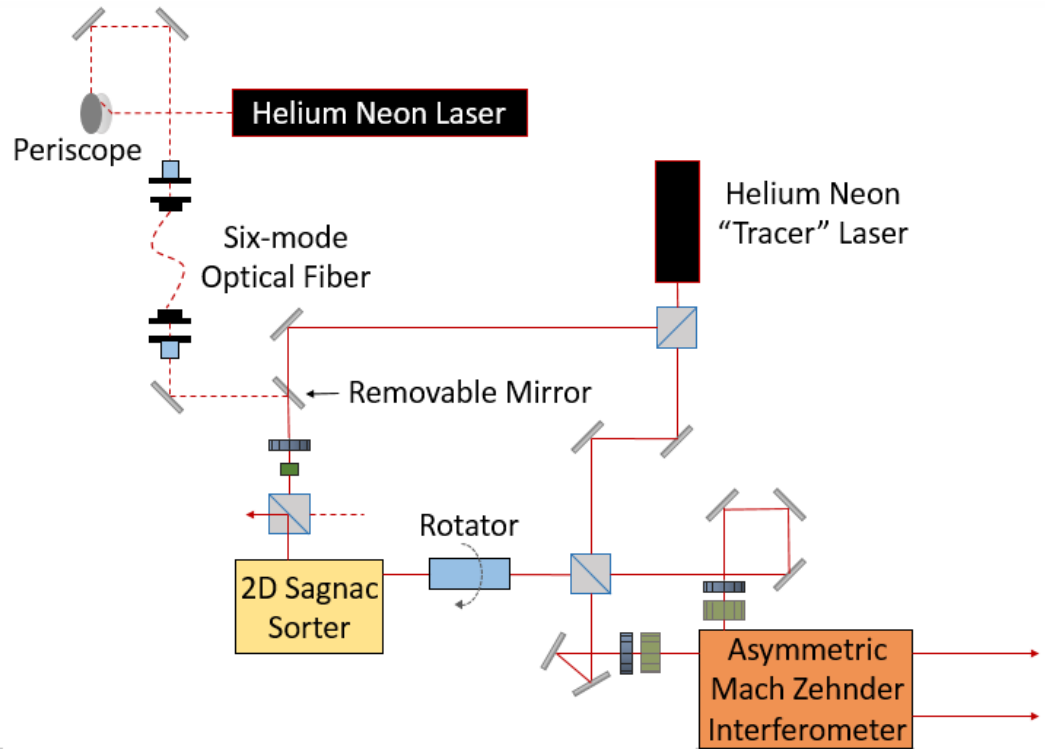


Figure 3.2: The Gaussian profile tracer laser simplifies the process of precision alignment of both the 2D Sagnac and asymmetric Mach-Zehnder interferometers. Although the original laser is off during the alignment process, the path it would take is still denoted by the dashed lines. The symbol key for this image is identical to the key in Fig. 2.6.

of the mode at various points. However, the amount of attenuation was not altered between measurements of individual experiments. Because the resulting images from the attenuated light were often very dim, most of the data images were enhanced by changing the color contrast after the fact. This does not alter the mode observed by the CCD, but simply makes it easier for the reader to see the difference between the bright and dim pixels.

3.2 HOM Interference Case of Interest

As we have seen in Section 2.2.2, HOM interference occurs in the asymmetric Mach-Zehnder interferometer only when the internal phase shifter is set at $\delta = \pm \frac{\pi}{2}$. For this reason, the we pay special attention to these cases in both theory and experiment.

3.2.1 Two-input theory

In the previous chapter, we discussed the general output of the asymmetric MZI given the condition that the inputs are identical. Here, let us discuss a specific dual-input case of

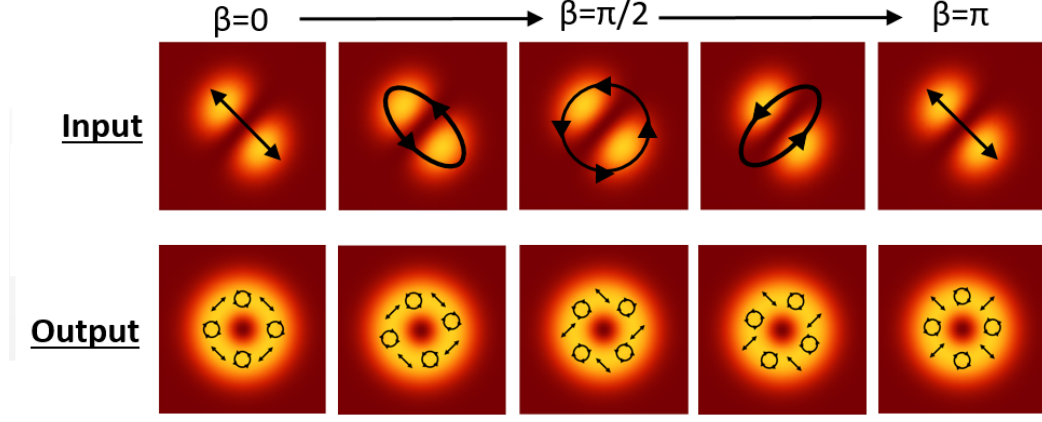


Figure 3.3: The intensity and polarization state of the theoretical inputs, satisfying the conditions $\theta = \frac{\pi}{2}$, $\phi = 0$, $\alpha = \frac{\pi}{2}$, and the output mode for port c is in the mode Ψ_- , which is shown. As the parameter β varies, the polarization state of the input changes from linear to circular to linear. However as β changes, the output spatially dependent polarization state rotates counterclockwise about the beam axis for the Ψ_- state.

interest: $\theta = \frac{\pi}{2}$, $\phi = 0$, $\alpha = \frac{\pi}{2}$, which is illustrated in Fig. 3.3. This input is interesting to us because there occurs the previously mentioned complete destructive interference effect in conjunction with the production of controllably varying nonseparable spin-orbit modes.

These nonseparable modes are particularly interesting for a couple of reasons. First, if these modes were used as quantum information carriers, they would carry two inseparable pieces of information: one from the spatial mode and one from polarization. Inseparable means that the modes produced are not product states, and therefore the polarization is dependent on the transverse polar angle of the spatial mode. This feature has the potential to add to qubit processing. Secondly, nonseparable spin-orbit modes have the potential to be used in optical tweezing. Here it might be useful to be able to easily change the polarization structure of the mode using only one parameter, as states in Section 2.1.7. We find that β can play that role in our interferometer. This parameter is simple to control, by tilting a wave plate or other birefringent crystal with respect to the beam axis, and has the ability to change the polarization structure of the output modes. For this purpose, we allow β to remain a variable.

Let's investigate this special case starting from the general output electric field function, Eqns. 2.44 and 2.45. First, we can see that the functions $A_{\pm}, B, M_{\pm}, R_{\pm}$ simplify giving

$$\begin{aligned}
 A_{\pm} &= \frac{1}{2} (\sin^2 \Phi \pm \cos^2 \Phi) \\
 B &= \frac{1}{2} \sin(2\Phi) \\
 M_{\pm} &= \pm \frac{1}{\sqrt{2}} \cos \Phi \\
 R_{\pm} &= \pm \frac{1}{\sqrt{2}} \sin \Phi.
 \end{aligned} \tag{3.2}$$

Using these values in Eqn. 2.44, we find that the output electric field function simplifies to

$$\vec{\mathbf{E}}\left(\frac{\pi}{2}, 0, \frac{\pi}{2}, \beta; \delta; \rho, \Phi\right) = \frac{1}{2} G(\rho) e^{\pm i\Phi} \left(\cos\left(\frac{\delta}{2}\right) \pm \sin\left(\frac{\delta}{2}\right) \right) [\hat{\mathbf{y}} \mp i e^{i[\beta \mp 2\Phi]} \hat{\mathbf{x}}]. \tag{3.3}$$

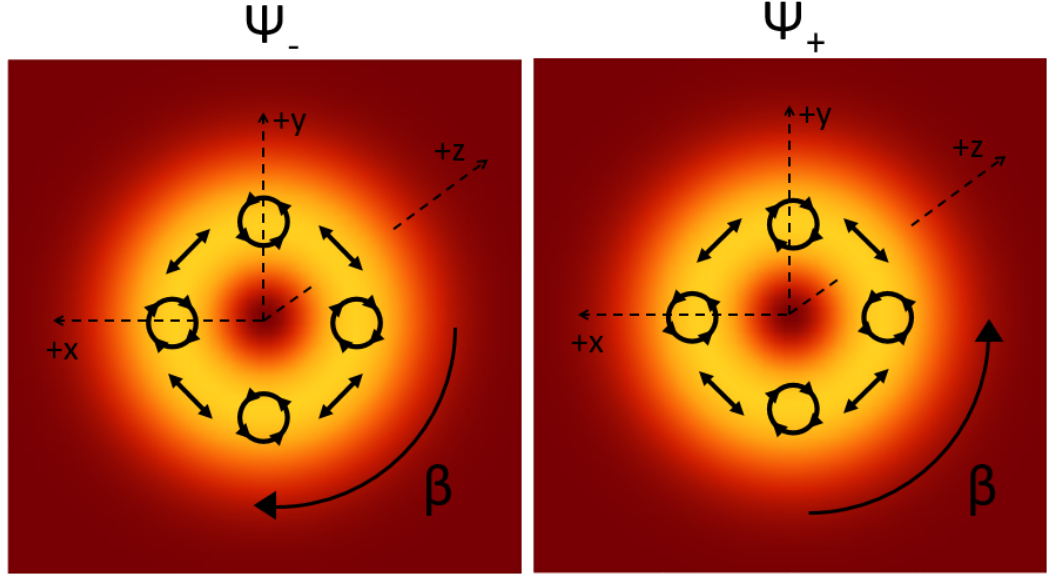


Figure 3.4: The outputs of the asymmetric MZI, Ψ_{\mp} , for $\theta = \frac{\pi}{2}$, $\phi = 0$, and $\alpha = \frac{\pi}{2}$. Here a select number of polarization states are superimposed onto the intensity graphs. Shown in dotted lines are the coordinate axes used throughout, where the perspective is looking along the $+z$ axis, in the direction of propagation. The effect of the parameter β is to rotate the polarization positions about the beam axis. Note that the circularity of the polarization and rotation effect of the parameter β between the two output functions is opposite.

Note that the δ parameter only changes the magnitude of the electric field function. As with the general case, the magnitude of the electric field is variable with δ , where the magnitude can be completely extinguished for each port with the choice of $\delta = \pm \frac{\pi}{2}$.

The function $G(\rho)$ is such that the electric field's magnitude is zero at $\rho = 0$, peaks, and then dies out exponentially as $\rho \rightarrow \infty$. The $e^{i\Phi}$ term can also be written as $\cos \Phi + i \sin \Phi$ and indicates that the electric field spirals through space. This circular symmetry is significant because it is fundamentally different from the input mode which oscillates about the line $x = y$. This can be called a mode transformation because the transverse electric field distribution has changed from the input to the output.

The polarization state of the mode is perhaps the most intriguing. Here we see that the polarization of the electric field in Eqn. 3.3 varies with both β and Φ . The Φ dependence means that the polarization changes with the transverse polar angle. In other words, the polarization of the mode is non-uniform and has radial symmetry. For each angle Φ of the mode, we encounter a different phase between the \hat{x} and \hat{y} components, making the polarization vary from linear through elliptical through circular and back again as the angle Φ changes.

The role of β in the polarization state is simple. This will change the relative phase between vertical and horizontal polarization for each polar angle Φ , effectively rotating the polarization structure about the beam axis. It is important to note that the direction of rotation is dependent on the function Ψ_{\mp} , which can be changed with port in the two-input

case or by choice of δ in the one-input case, represented by the choice of \pm in Eqn. 3.3. The output modes are shown in Fig. 3.4. The underlying polarization structure of the output mode, and the role of β in changing the structure is explored in the following experiments.

3.2.2 One-input Theory

While the two-input experiment holds interest in its correlation to the quantum biphoton HOM interference, the creation of nonseparable spin-orbit modes occurs for the one-input case as well, and is a simpler experiment.

Using the one-input theory from Section 2.1.6, we can set the internal phase shifter to $\delta = \pm\frac{\pi}{2}$, as is required to obtain the same functions as the two-input theory HOM interference requirements. Making this choice for Eqns. 2.36, and 2.37, we find that the two output electric fields are identical to each other, up to an overall phase that does not change measurable quantities, with the form

$$\vec{\mathbf{E}}_c = \vec{\mathbf{E}}_d \propto G(\rho)\Psi_{\mp}(\theta, \phi, \alpha, \beta; \rho, \Phi), \quad (3.4)$$

where Ψ_{\mp} is defined in Eqn. 2.40 as the output mode function for the Mach-Zehnder interferometer. In this case, however, the \pm index indicates whether the internal phase shifter, δ , is oriented at $+\frac{\pi}{2}$ or $-\frac{\pi}{2}$. It then becomes evident that the output modes of the Mach-Zehnder have identical forms with one input and two identical inputs. However, one-input experiments will never have the constructive and destructive interference patterns that show a classical analogy to HOM interference.

Since the single input demonstrates the electric field mode complexity using a simpler form of the experiment, the following data presented investigates the mode functions by collecting data for the single input case.

3.2.3 Testing the Spatially Varying Polarization Structure

This experiment is designed to investigate the underlying polarization structure of the output modes shown in Fig. 3.4. The polarization structure is not visible and does not manifest itself in the intensity distribution, but can be probed through the use of a linear polarizer placed after the output.

In this case, we will use our specific case of interest outlined in Section 3.2.1, where our input modes have the properties $\theta = \alpha = \frac{\pi}{2}$, $\phi = 0$, and fix $\beta = 0$ as shown in Fig. 3.5.

We then use a linear polarizer to learn about the polarization structure detailed in Fig. 3.4. The important piece, then, is to determine the output intensity distribution as a function of the linear polarizer angle. Using our special case input parameters and Eqn. 2.46, the general form of the output intensity for these identical inputs, we find that the output intensity is

$$I\left(\frac{\pi}{2}, 0, \frac{\pi}{2}, \beta; \delta; \rho, \Phi\right) = \frac{1}{\sqrt{2}} \frac{N}{w_0} \rho e^{-\left(\frac{\rho}{w_0}\right)^2} (1 \pm \sin \delta), \quad (3.5)$$

which is not dependent on either β , or Φ . This suggests that the intensity has circular symmetry, and indeed, the intensity of the mode is shown in Fig. 3.4.

The polarization of the mode shown in Fig. 3.4 can be measured in the lab using the technique described in the theory section. Here we found the change in intensity distribution of the output of the MZI when a linear polarizer is inserted before the detector and rotated through an angle Γ from the vertical. In our case of $\theta = \frac{\pi}{2}$, $\phi = 0$, $\alpha = \frac{\pi}{2}$, the intensity after

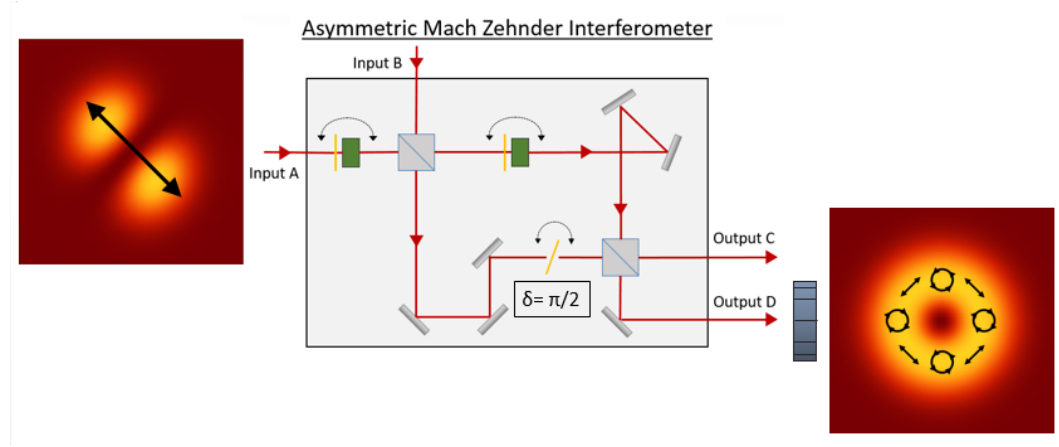


Figure 3.5: A schematic of the asymmetric Mach-Zehnder interferometer set-up for an experiment creating and testing a nonseparable spin-orbit mode using only one input. Note that the arrows on the input modes represent the polarization structure of the light, which is not visible. The output polarization structures can be investigated using the linear polarizer set after the output. The key is shown in Fig. 2.6.

the linear polarizer, Eqn. 2.50, simplifies to

$$I\left(\frac{\pi}{2}, 0, \frac{\pi}{2}, \beta; \delta; \rho, \Phi; \Gamma\right) = \frac{1}{4}G^2(\rho) [1 \pm \sin \delta] (1 \mp \sin(2\Gamma) \sin(\beta \mp 2\Phi)). \quad (3.6)$$

Let's analyze the intensity patterns after the linear polarizer, as shown in Table 3.1. Here if the orientation of the linear polarizer is vertical, the argument of the second square brackets is one and Eqn. 3.6 simplifies to Eqn. 3.5, which has circular symmetry and zero intensity in the center. This same intensity distribution should also appear at the linear polarizer angle $\Gamma = 90^\circ$, $\Gamma = 180^\circ$, and $\Gamma = 270^\circ$.

At polarizer angles $\Gamma = 45^\circ$, $\Gamma = 135^\circ$, $\Gamma = 225^\circ$, and $\Gamma = 315^\circ$ the intensity distribution will be dependent on Φ in such a way that it will be a rotated first order Hermite Gaussian mode.

When this experiment is aligned with one input, $\theta = \alpha = \frac{\pi}{2}$, and $\beta = \phi = 0$, in the manner described above, we produce results shown in Table 3.1. Here they are shown below the associated theoretical values, as viewed in the direction of propagation. It is evident here that the interference pattern theorized in Fig. 3.4 is underlying the output spatial modes from the interferometer.

However, there is some difference between the theorized values and experimental results for this first experiment. The most noticeable difference would be the asymmetries in the modes for polarizer angles $\Gamma = 0^\circ$, and $\Gamma = 90^\circ$. These asymmetries occur when the interference in the MZI is not ideal. The most effected piece of interference occurs in the underlying polarization patterns. Since the intensity of the mode after it passes through a linear polarizer is directly correlated to the polarization structure, asymmetries in the intensity distribution will occur when the interference is not ideal.

Another difference to notice is that the experimental results for polarizer angle $\Gamma = 45^\circ$ and $\Gamma = 135^\circ$ have a difference in intensity between the two lobes of the mode. This might indicate that the polarization is not exactly 45° , but could be oriented at a slightly different

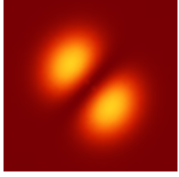
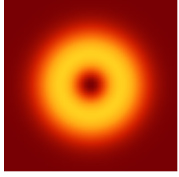
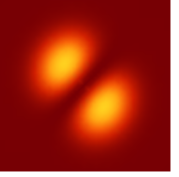
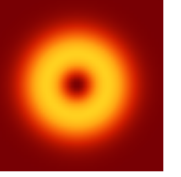
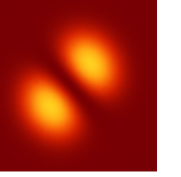
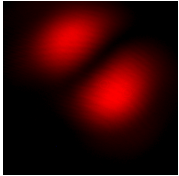
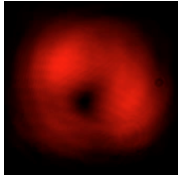
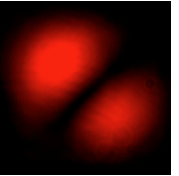
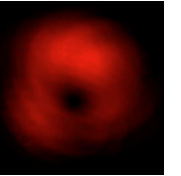
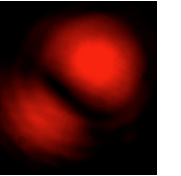
Theory				
Input	$\Gamma = 0^\circ$	$\Gamma = 45^\circ$	$\Gamma = 90^\circ$	$\Gamma = 135^\circ$
				
Experiment				
Input	$\Gamma = 0^\circ$	$\Gamma = 45^\circ$	$\Gamma = 90^\circ$	$\Gamma = 135^\circ$
				

Table 3.1: The results of the experiment designed to create and test nonseparable spin-orbit modes, $\theta = \alpha = \frac{\pi}{2}$, and $\phi = \beta = 0$. After the output port of the interferometer, a linear polarizer is placed and oriented at angle Γ . The upper row shows the theoretical predictions for the transverse intensity distribution of the light after passing through the linear polarizer. The bottom row shows the experimental outcome taken with a CCD camera.

angle or be elliptical.

These discrepancies are slight, but should be eliminated as much as possible in the future. The non-ideal interference is in part due to the quality of the beam-splitters. Each beam-splitter should reflect 50% of the light and transmit 50%. However, the products that we use for our experiment have an 8% tolerance, meaning that the reflected and transmitted percentages can vary by the tolerance amount [38]. Since there are two beam-splitters in our experiment, this has the potential to create substantial error. It would be useful to create a model of the interferometer with 42-58 beam-splitters, where 42% is reflected and 58% is transmitted and vice versa, to quantify the amount of error that we can expect with this apparatus.

A second contributor to the difference between experiment and theory comes from the misalignment of both the Sagnac interferometer and the Mach-Zehnder. While tracer lasers were used in order to align the internal components of each interferometer, the input angle of the light into each interferometer is critical for ideal alignment, the quality of which is largely up to the visible discretion of the experimenter for higher order input modes.

3.2.4 Observing Controllable Polarization Structure Changes

This second experiment is designed to test to role of β in the output polarization structure. To test this, the polarizer at the output is set to $\Gamma = 45^\circ$, and the input β parameter is varied. This experiment is shown pictorially in Fig. 3.6.

Because of the spacing of the optical elements in the experiment, we chose to place the Berek compensator that changes the β parameter after the outputs of our experiment.

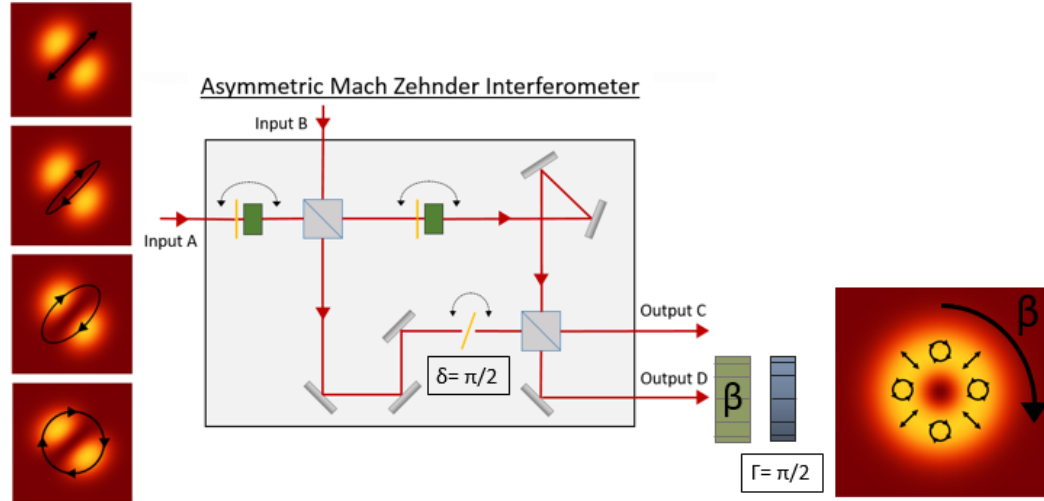


Figure 3.6: An experimental set-up to demonstrate the effect of β on the polarization state of the output modes. For experimental simplicity, the Berek compensator that changes β is placed at the output. As this parameter is changed, the polarization state of the output mode rotates around the beam axis. Note that the rotation direction is clockwise for the phase shifter angle $\delta = +\frac{\pi}{2}$. The key is shown in Fig. 2.6.

Since the β parameter is a phase between the \hat{x} and \hat{y} polarization components, it makes no difference in the theory whether it occurs at the input or the output, as long as it is applied before measurements are taken.

As shown in Table 3.2, when the linear polarizer at the output is oriented at $\Gamma = 45^\circ$ and $\beta = \pi$, the intensity distribution is a first order rotated Hermite Gaussian. As shown, at the cross-sectional mode angles $\Phi = \frac{\pi}{4}$ and $\Phi = -\frac{3\pi}{4}$, the linear polarizer completely extinguishes the light, meaning at these values of Φ , the polarization is orthogonal to the linear polarizer. As β is changed, the polar angles at which the extinguished line lies changes, indicating that the polarization oriented against the linear polarizer, changes its polar position on the mode. This effect is shown both theoretically and experimentally in Table 3.2, as predicted in Section 3.2.1.

It is evident from this table that our experimental results support our predictions. The mode rotating clockwise as the β parameter is changed indicates that the polarization structure underlying these modes is rotated clockwise around the beam axis.

This is strong evidence in support of controllable polarization structures occurring as predicted. However, there can always be improvement in these measurements. The line of completely extinguished light that runs through the modes shown in the theory are not completely extinguished in the experiment. This is especially apparent in the $\beta = \frac{3\pi}{2}$ measurement, where the black line does not pass completely through the upper region of the mode. This effect would occur when the polarization at this point is not exactly linear and oriented against the polarizer. As detailed in Section 3.2.3, this is most likely due to the imperfections in the beam-splitters or in misalignment of our apparatus.

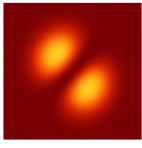
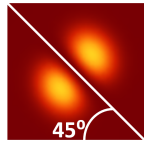
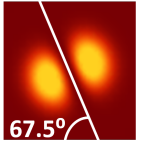
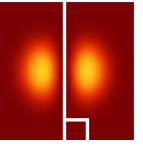
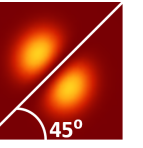
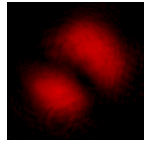
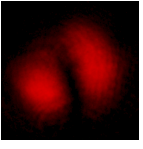
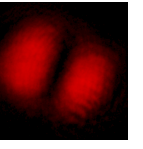
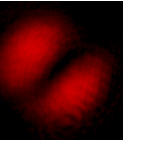
Theory					
Input	$\beta = \pi$	$\beta = \frac{5\pi}{4}$	$\beta = \frac{3\pi}{2}$	$\beta = \frac{7\pi}{4}$	$\beta = 2\pi$
					
Experiment					
Input	$\beta = \pi$	$\beta = \frac{5\pi}{4}$	$\beta = \frac{3\pi}{2}$	$\beta = \frac{7\pi}{4}$	$\beta = 2\pi$
					

Table 3.2: The comparison of theoretical predictions and experimental data representing an experiment that investigates the role of the parameter β in the structure of the polarization state, $\theta = \alpha = \frac{\pi}{2}$, $\phi = 0$, and $\delta = +\frac{\pi}{2}$. Here, a linear polarizer is set to 45° and the parameter β is changed. Shown is the transverse intensity distribution after passing through the linear polarizer for each case.

3.2.5 Investigating a Tunable Spatial Mode

The motivation behind this next experiment is to demonstrate output spatial mode variance by changing an input parameter instead of using a linear polarizer. This is worth consideration because these experiments will be performed in the future with single photons, and linear polarizers can cause significant photon loss.

Here we look at input first order Hermite Gaussian mode in state $\theta = \phi = \pi/2$, and polarization state $\beta = 0$ allowing α to vary. We have already shown that for the case where $\delta = \pm\frac{\pi}{2}$, the HOM interference condition, that both the one and two-input theory output the same wave function (Section 3.2.2). Thus, the following experiment will present the two-input theory as it is the most comprehensive and relevant, while testing the wave function by using the simpler one-input experiment. The set-up for the experiment is shown in Fig. 3.7.

Starting from Eqns. 2.44 and 2.45, where the assumption is identical dual inputs, we substitute our input parameters $\theta = \phi = \pi/2$ and $\beta = 0$ to get

$$\vec{\mathbf{E}}\left(\frac{\pi}{2}, \frac{\pi}{2}, \alpha, 0; \delta; \rho, \Phi\right) = G(\rho) \left(\cos\left(\frac{\delta}{2}\right) \pm \sin\left(\frac{\delta}{2}\right) \right) \left[\pm \cos\frac{\alpha}{2} \sin\left(\frac{\pi}{4} \pm \Phi\right) \hat{\mathbf{y}} + i \sin\frac{\alpha}{2} \sin\left(\frac{\pi}{4} \mp \Phi\right) \hat{\mathbf{x}} \right], \quad (3.7)$$

where the \pm refers to the output ports c, d respectively.

Next, the intensity function will vary with α , so that taking the dot product of the electric field with its complex modulus, we find the intensity is

$$I\left(\frac{\pi}{2}, \frac{\pi}{2}, \alpha, 0; \delta; \rho, \Phi\right) \propto G(\rho)^2 (1 \pm \sin \delta) [1 \pm \cos(\alpha) \sin(2\Phi)]. \quad (3.8)$$

Using Eqns. 3.7 and 3.8 we can determine both the intensity distribution and polarization structure of these modes as α is varied. At $\alpha = 0$, the intensity is zero at polar mode angles

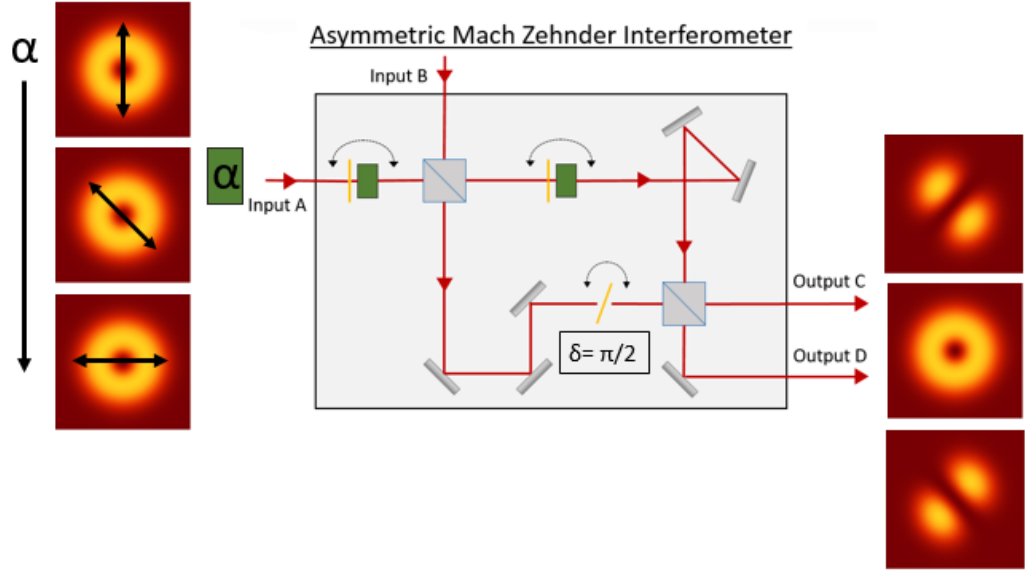


Figure 3.7: The set-up for an experiment where the interferometer output intensities can be controllably varied by changing the angle of the input linear polarization. This polarization angle, α , is controlled using a half-wave plate at the input of the interferometer. The key is shown in Fig. 2.6.

$\Phi = \pm \frac{\pi}{4}$ depending on the output port. This means that the intensity distribution is the same as a first order Hermite Gaussian mode oriented at $\pm 45^\circ$ depending on the port. At $\alpha = 0$, the output polarization is uniform \hat{y} according to Eqn. 3.7. This is shown in Table 3.3.

For input $\alpha = \frac{\pi}{2}$, the Φ dependence in Eqn. 3.8 is removed, leading to cylindrically symmetric intensity distribution. However, the function $G(\rho)$ has the value zero at $\rho = 0$, and $\rho = \infty$. This intensity distribution is identical to the input intensity distribution and is shown in Fig. 3.3. The polarization structure for this output, however is non-uniform, and is shown also in Fig. 3.3.

For input $\alpha = \pi$, the output mode is again a rotated Hermite Gaussian spatial mode, but is rotated in the opposite direction from $\alpha = 0$. However, for this value of α , the electric field equation tells us that the polarization is uniform \hat{x} , as shown in Table 3.3.

The experiment in Fig. 3.7 uses a half wave plate to change the polarization of the inputs (α), in place of a linear polarizer, in order to observe the change in spatial intensity distribution. However, in our physical set-up, we found it necessary to add a linear polarizer before the half wave plate in order to remove any phases that the light picks up from the mirror reflections in the Sagnac interferometer, rotator, and input alignment mirrors. The addition of this single linear polarizer resolves this issue.

The results of this experiment are shown in Table 3.4 alongside the theoretical predictions outlined above. For this experiment, the output modes are significantly more cylindrically symmetric than in the first experiment. This could potentially be due to the lack of linear polarizer before the detector, which often brings to light imperfect interference in the

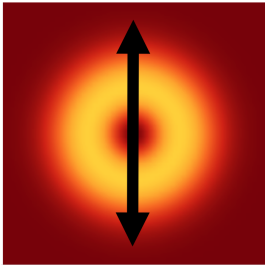
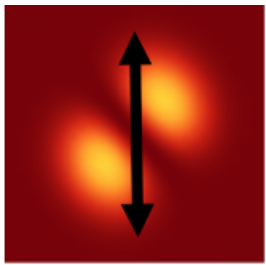
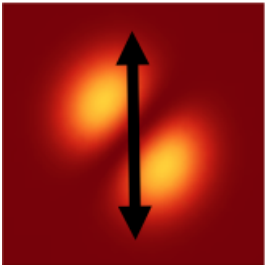
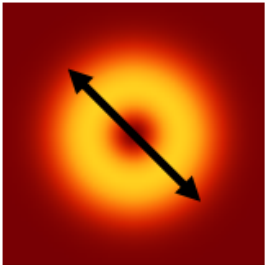
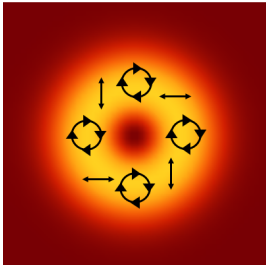
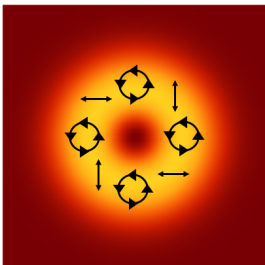
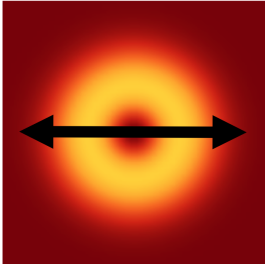
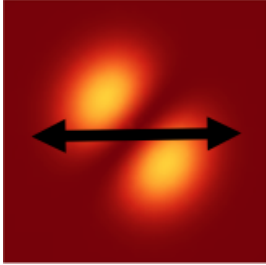
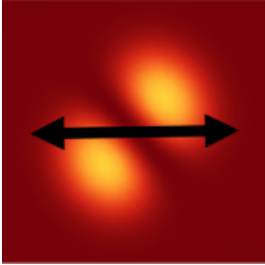
Input	Ψ_+	Ψ_-
$\alpha = 0$ 		
$\alpha = \pi/2$ 		
$\alpha = \pi$ 		

Table 3.3: The theoretical predictions of the input-output relations for the experiment designed to control the output intensity distribution using only the parameter α . Notice that the inputs must have a circularly symmetric intensity distribution, and the polarization state remains unchanged for linear vertical and horizontal input polarizations.

polarization state.

A couple of differences between theory and experiment that are worth noting is the angle and shape of the line of zero intensity across the first and third measurements in Table 3.4. The dark line through the first measurement appears to be at a slightly different angle than theoretically predicted. This is effected by the angle of the glass plate in the one-input case. Recall that the output wave functions are only identical for the case where the glass plate is set to $\delta = \pm \frac{\pi}{2}$. For our experimental purposes, we cannot measure the precise angle at which to set the glass plate in order to produce an internal phase shift of $\frac{\pi}{2}$. Instead we use drawings in the CCD camera program that show vertical, horizontal, and

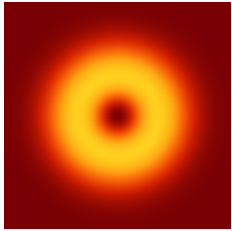
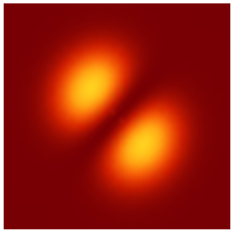
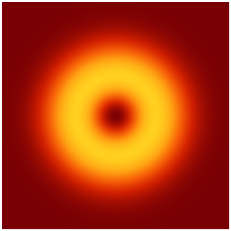
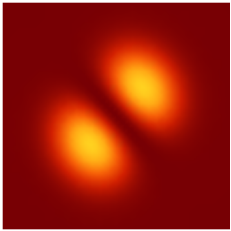
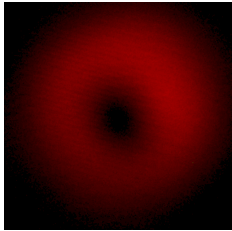
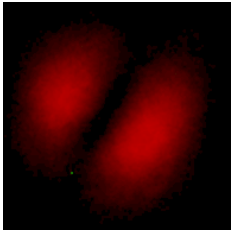
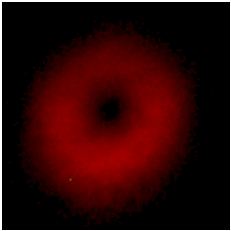
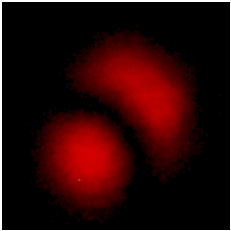
Theory			
Input	$\alpha = 0$	$\alpha = \frac{\pi}{2}$	$\alpha = \pi$
			
Experiment			
Input	$\alpha = 0$	$\alpha = \frac{\pi}{2}$	$\alpha = \pi$
			

Table 3.4: The intensity distributions of the outputs of the MZI with input parameters $\theta = \phi = \frac{\pi}{2}$, $\beta = 0$. The upper set of figures show the theoretical predictions and the lower set show the experimental data. The similarity between the two demonstrates that the spatial mode can be varied by changing only the input polarization, demonstrating the interdependence of the two degrees of freedom.

45° angles, as shown in Fig. 3.8, and we rotate the glass plate until the output mode aligns with the expected orientation, with viewer discretion. For this reason, there is error in the measurement of the angle of the zero intensity line. This could be improved using a simple computer program that would analyze the intensity of each pixel from the CCD in real time and measure the angle at which the pixel intensity is zero compared to its surroundings.

Another issue that has arisen in setting the glass plate to $\delta = \frac{\pi}{2}$ has been its stability. At the moment, this glass plate stands about a centimeter tall over its fixed point on a rotation stage, making the glass plate susceptible to vibrational fluctuations in the table, and to air currents in the room. This means that if an experiment is not performed quickly, the glass plate will move slightly, contributing to imperfections in the data, possibly contributing to the bend in the dark line of zero intensity through the third measurement in Table 3.4.

A final experiment that could be done in the future would be to verify the polarization structure of the modes presented in Table. 3.3. This could be done by adding a linear polarizer at the output of the MZI set-up shown in Fig. 3.7, and rotating it to see if the intensity distribution or power changes at different polarizer angles.

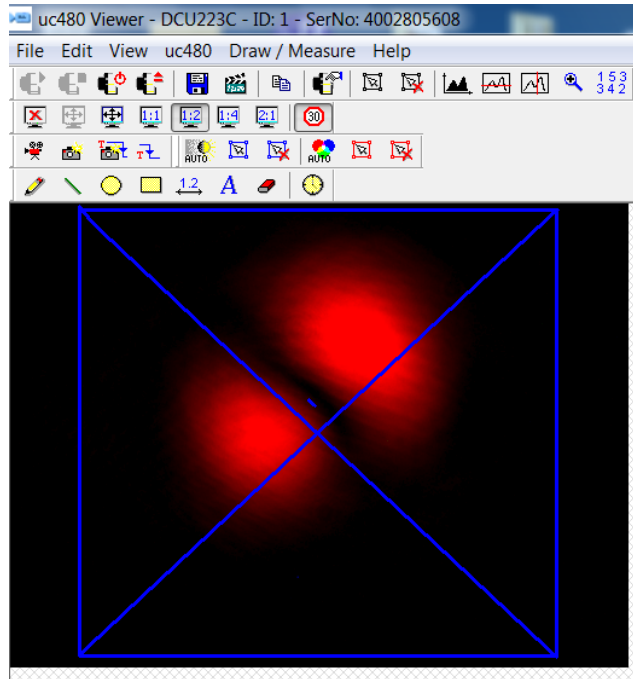


Figure 3.8: The CCD camera interface program that is used to take data. Here the blue lines show the drawing that can be loaded into the viewer as the camera is playing in real time to indicate vertical, horizontal, and 45° angles.

3.3 Additional Spatially Varying Polarization Structures

The intricate polarization states that we have found for the HOM interference case of interest, $\delta = \pm \frac{\pi}{2}$, could be useful for a couple of different applications. There has been some work done in the past couple of years where information from the spatial mode of light is encoded onto cold atoms and used as quantum repeaters and used to investigate the degree of entanglement of those cold atoms [12, 39, 40].

Another possible application for these types of modes would be to use them in an optical trap, such as optical tweezing, where the intricate polarization state would effect each trapped particle in a different way, depending on the polar mode angle at which it was trapped. The polarization of the light in an optical trap effects the spin angular momentum of the trapped particles [3]. In the previous cases investigated, the polarization structure would change when one of the input parameters, β or α , was varied, which in practice is very simple. If these modes were used in an optical trap, varying this one parameter would change the spin angular momentum of the particles trapped.

Since these kinds of structures are something that could be of use in a broader context, we investigate if there exist other exotic modes output from this asymmetric MZI in which the polarization and spatial degrees of freedom are nonseparable. We also investigate if any of these cases where changing the parameter β affects the polarization state in a controllable way.

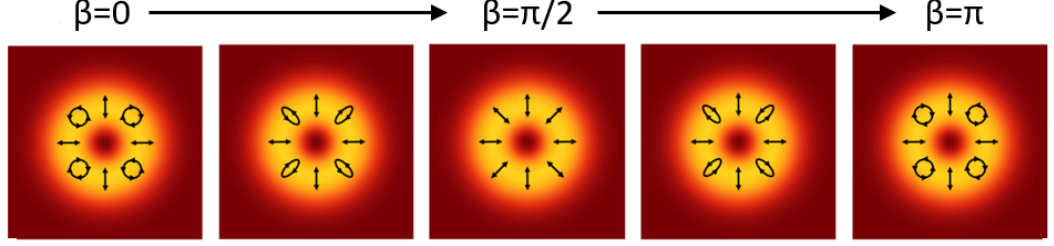


Figure 3.9: The change in the output polarization structure as β is varied for the condition $\theta = \alpha = \frac{\pi}{2}$, $\phi = \frac{\pi}{2}$, and $\delta = 0$. It can be seen that the change in this single parameter varies the polarization structure in such a way that polarization is constant at $\Phi = 0$, $\Phi = \frac{\pi}{2}$, $\Phi = \pi$, and $\Phi = \frac{3\pi}{2}$, while the other points vary from circular to linear polarization.

Since the input parameter space that allows HOM interference to occur has been sufficiently explored, the next logical step is to investigate the output modes of the asymmetric MZI when the HOM condition is not met. We have discovered that the critical factor for HOM interference is that the internal phase shifter must be set to $\delta = \pm\frac{\pi}{2}$. However, in the following section, we will investigate an asymmetric MZI with one input and internal phase shifter angle $\delta = 0$, or $\delta = \pi$.

It is possible to design a case where the output polarization structure varies with transverse polar angle Φ , similar to the output modes that occur in conjunction with HOM interference. It is also possible that there will be a similar case in which the parameter β plays an important role in changing the polarization state of the output modes. However, in the case where $\delta = 0$, we will not have rotation of the overall polarization state about the beam axis. Here, the role of β will be to change the polarization state at some transverse polar angles while leaving others unchanged. The proposed experiment will see the polarization change in the manner shown in Fig. 3.9, where polarization states at key angles of $\Phi = 0$, $\Phi = \frac{\pi}{2}$, $\Phi = \pi$, and $\Phi = \frac{3\pi}{2}$ remain unchanged as all other angles experience a transformed polarization.

Starting from the general one-input theory, concluded in Eqns. 2.36 and 2.37, we can find the cases where spatially varying polarization would occur. First we can choose $\delta = 0$ to show our new condition. This will simplify the two equations into

$$\begin{bmatrix} \vec{\mathbf{E}}_c \\ \vec{\mathbf{E}}_d \end{bmatrix} \propto G(\rho) \begin{bmatrix} \sin(\frac{\theta}{2}) \cos(\frac{\alpha}{2}) \cos \Phi \hat{\mathbf{y}} + e^{i\beta-\phi} \cos(\frac{\theta}{2}) \sin(\frac{\alpha}{2}) \sin \Phi \hat{\mathbf{x}} \\ \cos(\frac{\theta}{2}) \cos(\frac{\alpha}{2}) \sin \Phi \hat{\mathbf{y}} + e^{i\beta+\phi} \sin(\frac{\theta}{2}) \sin(\frac{\alpha}{2}) \cos \Phi \hat{\mathbf{x}} \end{bmatrix}, \quad (3.9)$$

where the two outputs are represented as a column vector, and an overall phase of $\pm e^{-\phi}$ factors out of the $\vec{\mathbf{E}}_c$ term, and an overall phase of $\pm i$ factors out of the $\vec{\mathbf{E}}_d$ term. Here the choice of sign for the overall factors represent the choice of $\delta = 0$ or $\delta = \pi$.

The most interesting cases of output modes involve an interdependence of the polarization state and the spatial mode. This can occur in the above equation when $\alpha = \pm\pi/2$ and $\theta = \pm\pi/2$. We will look at these specifically because these values produce output nonseparable spin-orbit modes.

This further simplifies our case of interest to simply

$$\begin{bmatrix} \vec{\mathbf{E}}_c \\ \vec{\mathbf{E}}_d \end{bmatrix} \propto G(\rho) \begin{bmatrix} \pm \cos \Phi \hat{\mathbf{y}} + e^{i\beta-\phi} \sin \Phi \hat{\mathbf{x}} \\ \pm \sin \Phi \hat{\mathbf{y}} + e^{i\beta+\phi} \cos \Phi \hat{\mathbf{x}} \end{bmatrix}, \quad (3.10)$$

where the sign choice indicates +1 if $\alpha = \theta = \pi/2$ and -1 if $\alpha = -\theta = \pi/2$. In our experiment, we choose the case where $\alpha = \theta$, which simply eliminates the \pm choice in the above equation.

Depending on the choice of β and ϕ , the polarization state will be in various combinations of linear and elliptical, all varying with transverse polar angle Φ . In the previous experiments, we used a linear polarizer to determine the structure of the underlying polarization state. However, the linear polarizer does not distinguish between linear 45° polarization and circular polarization. In this experiment, we will see that by changing one input parameter, we can change circular polarization into linear 45° and back, as shown in Fig. 3.9. Therefore to be able to measure the difference in polarization state we must use something other than a linear polarizer.

Stokes parameters are often used to describe the polarization of light, in which values are measured that describe the intensity of the light, its degree of polarization, and the orientation and circularity of the polarization [41]. Inspired by these parameters, we found that we could take a measurement involving the circularity of the polarization to distinguish between clockwise and counter-clockwise circular polarization. This measurement involves using a combination of quarter wave plate oriented at 45° and a polarizing beam splitter. The quarter wave plate would transform circular polarization into linear, and the polarizing beam splitter would sort the two linear components. This set-up is shown in Fig. 3.10. The idea of this stokes measurement is that we determine the circularity of the polarization through the use of a quarter wave plate. If the fast axis is oriented at 45° clockwise from vertical when looking in the direction of propagation, clockwise circular polarization will be transformed into $\hat{\mathbf{x}}$ while counterclockwise circular polarization will be transformed into $\hat{\mathbf{y}}$. Finally, as the 45° linear polarization is aligned completely along the fast axis of the crystal, it sees no change. In this way we can distinguish between linear 45° , clockwise circular and counterclockwise circular.

The most common way to transform a mathematical polarization vector is through the use of Jones matrices [41]. Here we construct a matrix that acts on the polarization components in a vector with the $\hat{\mathbf{x}}$ polarization in the first entry. First we find a matrix that will retard the $\hat{\mathbf{x}}$ polarization by a quarter wave with respect to the $\hat{\mathbf{y}}$ polarization. This matrix could be written as

$$\hat{\mathbf{W}}\mathbf{P} = \begin{bmatrix} e^{i\pi/2} & 0 \\ 0 & 1 \end{bmatrix} = \begin{bmatrix} i & 0 \\ 0 & 1 \end{bmatrix}. \quad (3.11)$$

A rotation matrix can be found in the coordinate axes described above to be

$$\hat{\mathbf{R}}(\theta) = \begin{bmatrix} \cos(\theta) & \sin(\theta) \\ -\sin(\theta) & \cos(\theta) \end{bmatrix}, \quad (3.12)$$

where θ is the rotation of the optical element.

With these two matrices, we can build our Jones matrix for a quarter wave plate oriented at angle θ as follows [41],

$$\hat{\mathbf{R}}(\theta) \times \hat{\mathbf{W}}\mathbf{P} \times \hat{\mathbf{R}}(\theta)^{-1} = \begin{bmatrix} \sin^2(\theta) + i \cos^2(\theta) & (1-i) \sin(\theta) \cos(\theta) \\ (1-i) \sin(\theta) \cos(\theta) & \cos^2(\theta) + i \sin^2(\theta) \end{bmatrix}, \quad (3.13)$$

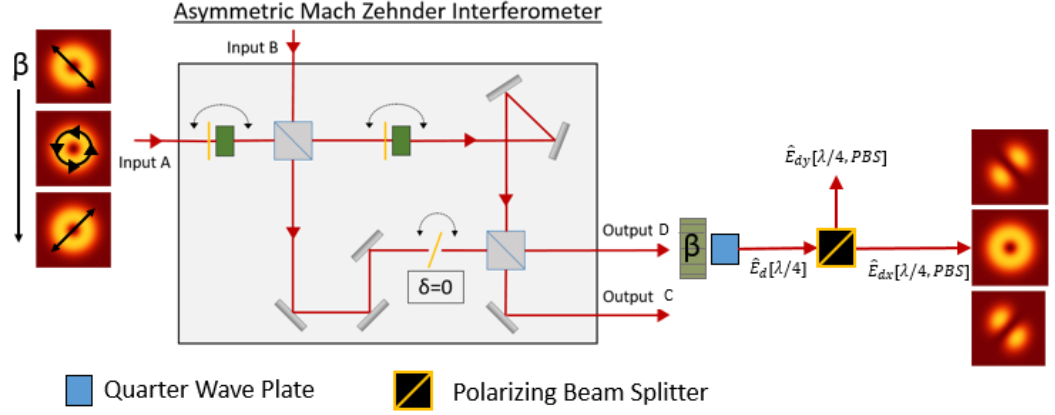


Figure 3.10: The set-up for an experiment testing the role of β for a case where $\delta = 0$. The notation describing the electric field as it passes through each element beyond the MZI is shown here for port D. Since a linear polarizer cannot distinguish between circular and linear 45° , a combination of quarter wave plate and polarizing beam splitter is used to measure the polarization state of the output.

which reduces to

$$\sqrt{2} e^{i\pi/4} \begin{bmatrix} 1 & -i \\ -i & 1 \end{bmatrix} \quad (3.14)$$

for a rotation angle of 45° as we use in our experiment [32].

Next we need to apply this Jones matrix to the electric field outputs of the Mach-Zehnder interferometer. Previously we have written the outputs in a column vector which represents each of the two output ports. Here, however, we must use the Jones vector convention of breaking apart each electric field into two polarization components,

$$\begin{aligned} \hat{\mathbf{E}}_c &\propto G(\rho) \begin{bmatrix} e^{i(\beta-\phi)} \sin \Phi \\ \cos \Phi \end{bmatrix}, \\ \hat{\mathbf{E}}_d &\propto G(\rho) \begin{bmatrix} e^{i(\beta+\phi)} \cos \Phi \\ \sin \Phi \end{bmatrix}. \end{aligned} \quad (3.15)$$

Here the subscripts c and d refer to the electric field from output port c and d respectively. Since the next optical element that the light encounters (see Fig. 3.10) is the half wave plate, we multiply the polarization Jones vectors on the left by the quarter wave plate Jones matrix, as described in Eqn. 3.14. This leads to

$$\begin{aligned} \hat{\mathbf{E}}_c[\lambda/4] &\propto \begin{bmatrix} 1 & -i \\ -i & 1 \end{bmatrix} \begin{bmatrix} e^{i(\beta-\phi)} \sin \Phi \\ \cos \Phi \end{bmatrix} = \begin{bmatrix} e^{i(\beta-\phi)} \sin \Phi - i \cos \Phi \\ -ie^{i(\beta-\phi)} \sin \Phi + \cos \Phi \end{bmatrix}, \\ \hat{\mathbf{E}}_d[\lambda/4] &\propto \begin{bmatrix} 1 & -i \\ -i & 1 \end{bmatrix} \begin{bmatrix} e^{i(\beta+\phi)} \cos \Phi \\ \sin \Phi \end{bmatrix} = \begin{bmatrix} e^{i(\beta+\phi)} \cos \Phi - i \sin \Phi \\ -ie^{i(\beta+\phi)} \cos \Phi + \sin \Phi \end{bmatrix}, \end{aligned} \quad (3.16)$$

where the notation $[\lambda/4]$ denotes that the light has passed through the quarter wave plate, as shown in Fig. 3.10.

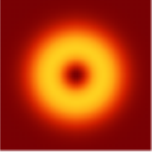
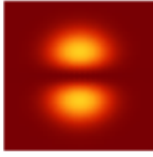
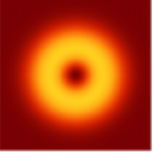
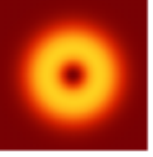
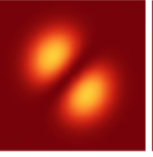
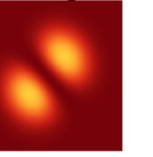
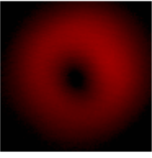
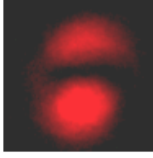
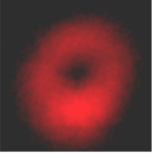
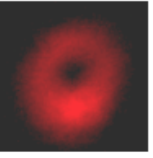
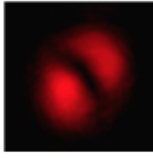
Theory					
Input	$\alpha = 0$	$\alpha = \frac{\pi}{2}$	Wave Plate	PBS $\hat{\mathbf{x}}$	
				$\phi = \frac{\pi}{2}$	$\phi = -\frac{\pi}{2}$
					
Experiment					
Input	$\alpha = 0$	$\alpha = \frac{\pi}{2}$	Wave Plate	PBS $\hat{\mathbf{x}}$	
					

Table 3.5: The output of the MZI port d with $\delta = 0$. Each column shows a step in the process of determining if the $\phi = +\frac{\pi}{2}$ or $\phi = -\frac{\pi}{2}$. The second and third columns show the output of the MZI directly when the parameter $\alpha = 0$, and $\alpha = \frac{\pi}{2}$ respectively. The fourth column shows the output when $\alpha = \frac{\pi}{2}$ and the light has passed through a quarter wave plate oriented at 45° . The final column shows the two possible outputs of the polarizing beam splitter for $\alpha = \frac{\pi}{2}$ after the light has passed through both the quarter wave plate and the polarizing beam splitter. It is shown through this set of measurements that the experimental input parameter is $\phi = -\frac{\pi}{2}$.

The next optical element that the light encounters in the experimental setup is a polarizing beam splitter. This is simply a beam splitter that allows light with polarization $\hat{\mathbf{x}}$ to transmit directly through and reflects light that has $\hat{\mathbf{y}}$ polarization. Since the $\hat{\mathbf{y}}$ polarized light is reflected, it will pick up an overall phase of i with respect to the transmitted light.

The outputs of the polarizing beam splitter can then be written as

$$\begin{aligned}
 E_{cx}[\lambda/4, PBS] &\propto G(\rho) \left[e^{i(\beta-\phi)} \sin \Phi - i \cos \Phi \right] \hat{\mathbf{x}} \\
 E_{cy}[\lambda/4, PBS] &\propto iG(\rho) \left[\cos \Phi - ie^{i(\beta-\phi)} \sin \Phi \right] \hat{\mathbf{y}} \\
 E_{dx}[\lambda/4, PBS] &\propto G(\rho) \left[e^{i(\beta+\phi)} \cos \Phi - i \sin \Phi \right] \hat{\mathbf{x}} \\
 E_{dy}[\lambda/4, PBS] &\propto iG(\rho) \left[\sin \Phi - ie^{i(\beta+\phi)} \cos \Phi \right] \hat{\mathbf{y}}, \tag{3.17}
 \end{aligned}$$

where the notation $E_{cx}[\lambda/4, PBS]$ means that the light exited port c of the Mach-Zehnder interferometer, passed through the quarter wave plate and exited the $\hat{\mathbf{x}}$ side of the polarizing beam splitter. For pictorial representation of this notation see Fig. 3.10.

The last piece of the puzzle is to analyze the intensity distribution of each of these functions because that is measurable. As before, the intensity of the light is defined to be

the complex modulus squared of the electric field function. This means that we can write the intensity functions as

$$\begin{aligned}
I_{cx}[\lambda/4, PBS] &= E_{cx}E_{cx}^* \propto G^2(\rho) [1 - \sin(\beta - \phi) \sin(2\Phi)], \\
I_{cy}[\lambda/4, PBS] &= E_{cy}E_{cy}^* \propto G^2(\rho) [1 + \sin(\beta - \phi) \sin(2\Phi)], \\
I_{dx}[\lambda/4, PBS] &= E_{dx}E_{dx}^* \propto G^2(\rho) [1 - \sin(\beta + \phi) \sin(2\Phi)], \\
I_{dy}[\lambda/4, PBS] &= E_{dy}E_{dy}^* \propto G^2(\rho) [1 + \sin(\beta + \phi) \sin(2\Phi)].
\end{aligned} \tag{3.18}$$

Now that we have all the pieces to analyze our experiment, we must determine the input parameter ϕ . In practice, the method of changing the parameter ϕ is to put stresses and torsion on the optical fiber, and analyze the odd output of the Sagnac sorter (which shows us the modes that are odd with respect to 180° rotation). This is done visually, and is up to the discretion of the experimenter. In Fig. 2.4, we can see the difference in modes as we move across the Bloch Sphere, and we find that if we move around the equator, we cannot tell the difference in intensity distribution between points $\theta = \frac{\pi}{2}, \phi = \frac{+\pi}{2}$ and $\theta = \frac{\pi}{2}, \phi = \frac{-\pi}{2}$. Therefore, after we have visually established that the input mode is one of the two, we have designed a quick test to determine which of the two inputs is being used.

This test consists of setting the input parameter α to zero, and rotating the glass plate until we find the output mode orientation that is associated with the glass plate angle $\delta = 0$, as shown in Table 3.5. We then quickly change the input linear polarization to $\alpha = \frac{\pi}{2}$, and insert both the quarter wave plate oriented at 45° and polarizing beam splitter after the Mach-Zehnder output and before the camera. Using Eqn. 3.9, we can see that the electric fields, and consequently the intensity distributions would be changed by a mirror image flip if the sign of ϕ is changed. Using this to our favor, we can solve for each case as described, and determine the value for ϕ . Each step of this process is shown pictorially in Table 3.5, and from this we can determine that $\phi = -\frac{\pi}{2}$.

Now that we have determined the value of ϕ for our experiment, we can simplify Eqns. 3.10, and 3.18 so that they are only functions of varying input parameter β , and transverse mode coordinates ρ and Φ .

The original output electric field is then

$$\begin{bmatrix} \vec{\mathbf{E}}_c \\ \vec{\mathbf{E}}_d \end{bmatrix} \propto G(\rho) \begin{bmatrix} \cos \Phi \hat{\mathbf{y}} + ie^{i\beta} \sin \Phi \hat{\mathbf{x}} \\ \sin \Phi \hat{\mathbf{y}} - ie^{i\beta} \cos \Phi \hat{\mathbf{x}} \end{bmatrix}, \tag{3.19}$$

and the final output intensity after the quarter wave plate and the polarizing beam splitter is then

$$\begin{aligned}
I_{cx}[\lambda/4, PBS] &\propto G^2(\rho) [1 - \cos(\beta) \sin(2\Phi)], \\
I_{cy}[\lambda/4, PBS] &\propto G^2(\rho) [1 + \cos(\beta) \sin(2\Phi)], \\
I_{dx}[\lambda/4, PBS] &\propto G^2(\rho) [1 + \cos(\beta) \sin(2\Phi)], \\
I_{dy}[\lambda/4, PBS] &\propto G^2(\rho) [1 - \cos(\beta) \sin(2\Phi)].
\end{aligned} \tag{3.20}$$

Using these two equations, we can put together case studies for the electric field and intensity after each optical device. These cases are shown in Fig. 3.6. In this way we can measure the polarization structure of each mode by using the CCD to image the intensity distribution after the polarizing beam splitter.

The data taken to give experimental support of this theory is shown in Table. 3.7. Here we chose to look at Mach-Zehnder output d and the \hat{x} output port of the polarizing beam splitter. Even though this is a small fraction of the data available to show the effect, it is a comprehensive set of data that supports our findings. Taking the experimental predictions for this set of data, shown in Fig. 3.6, we can compile a table that shows both the theoretical predictions and the experimental results of this case.

This table shows experimental evidence that changing the input parameter β will change the polarization structure of the Mach-Zehnder output modes in the way shown in Fig. 3.9.

There is, of course, some error in these measurements. The small circular interference fringes in the top left corner of each image come from a piece of dust on the glass plate. In this case, the majority of the difference between theory and experiment comes from the parameter ϕ . Since we have not set up an experiment to precisely measure the Bloch Sphere angle ϕ , we are using the visual discretion of the experimenter. It is possible to write a program that would compare the pixel intensity from the camera and compare with any linear combination of first order Hermite Gaussian modes to find more precise values of ϕ at the output of the Sagnac interferometer. Being able to measure and fine-tune the parameter ϕ would be a good next step to improve the apparatus. However, we show experimental evidence of another type of controllable spatially varying polarization state, which has a variety of application.

AMZI Output Port C, $\beta = 0$			
Original	Wave Plate	PBS \hat{x}	PBS \hat{y}
AMZI Output Port D, $\beta = 0$			
Original	Wave Plate	PBS \hat{x}	PBS \hat{y}
AMZI Output Port C, $\beta = \frac{\pi}{2}$			
Original	Wave Plate	PBS \hat{x}	PBS \hat{y}
AMZI Output Port D, $\beta = \frac{\pi}{2}$			
Original	Wave Plate	PBS \hat{x}	PBS \hat{y}
AMZI Output Port C, $\beta = \pi$			
Original	Wave Plate	PBS \hat{x}	PBS \hat{y}
AMZI Output Port D, $\beta = \pi$			
Original	Wave Plate	PBS \hat{x}	PBS \hat{y}

Table 3.6: The theoretical outputs of the MZI for $\theta = \alpha = -\phi = \frac{\pi}{2}$. The first column shows the original output spatial and polarization structure. The second column shows the change in polarization structure after the light has passed through a quarter wave plate oriented at 45° , and the last two columns show the change in spatial mode as the light travels from quarter wave plate out through the polarizing beam splitter. The experimental setup is shown in detail in Fig. 3.10.

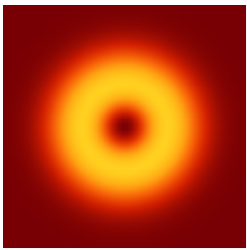
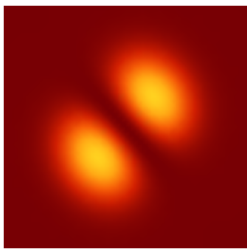
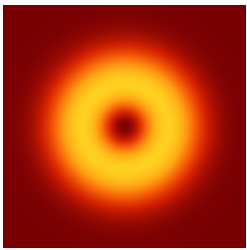
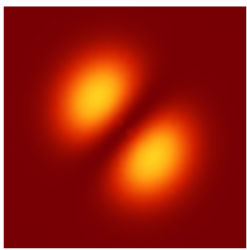
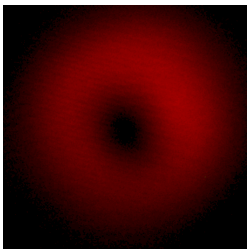
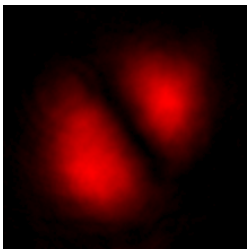
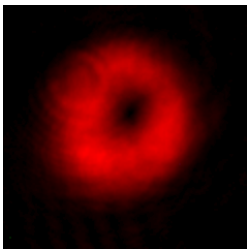
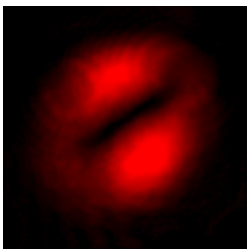
Theory			
Input	$\beta = 0$	$\beta = \frac{\pi}{2}$	$\beta = \pi$
			
Experiment			
Input	$\beta = 0$	$\beta = \frac{\pi}{2}$	$\beta = \pi$
			

Table 3.7: The comparison between the theory and experiment for the case where $\theta = \alpha = -\phi = \frac{\pi}{2}$, and $\delta = 0$ for out MZI port d , and polarizing beam splitter port \hat{x} . This change in output intensity distribution is evidence that the underlying polarization structure of the outputs for this case change as predicted and shown in Fig. 3.9.

Chapter 4

Conclusions

We have shown that an asymmetric Mach-Zehnder interferometer with an extra mirror in one arm can exhibit HOM interference given that the two inputs are identical. In addition, we demonstrate that for a given choice of inputs, the interferometer transforms light from a product mode, to a nonseparable spin-orbit mode. Since these two phenomena are independently valuable to multiple fields of study, we postulate that the two occurring simultaneously poses greater potential for application with a larger scope.

Application for nonseparable spin-orbit modes extend into the fields of chemistry and biology. In optical traps, polarization is used to transfer angular momentum to particles [3]. Therefore, controllable polarization that varies across a spatial mode could be useful for more elaborate systems. With spatially varying polarization, particles trapped in different areas of the optical trap would have different angular momentums imposed on them. We have shown that there is one global variable that will change the polarization structure of the interferometer output in a smooth, controllable manner. This global variable would then be able to control and change the angular momentum imposed on each trapped particle. This has applications in fields from condensed matter to molecular biology [5], and optical traps have been a way to study biological matter from human blood cells to E. coli viruses without significant damage to the cell structure [4]. Application for HOM interference ranges from studies in quantum entanglement to quantum computation and encryption. Given the value of each phenomena, the application of the two together opens the door to future discovery.

As with any scientific study, there is room to push beyond this work and create more experiments, and exploration. The next step in the investigation of these effects includes investigating the two-input case experimentally. We have shown that the output classical electric field functions are identical for one and two-input cases, however, we have not shown experimental evidence for the complete destructive interference effect that occurs in conjunction with mode conversion. Some experimental evidence to support the classical interference effect related to HOM interference is shown in [17], however, a more in depth exploration is needed to demonstrate the effect.

Another improvement to the experiment would be to design a computational program that would analyze the intensity of each CCD pixel and compare the pixel image to the theoretical prediction. This would be useful in quantifying how ideal the interference is, and could lead to improved analysis of our experimental results. A polarimeter could also be utilized in order to obtain more precise measurements of the polarization states at each point on the modes.

In general, the methods described in alignment and mode preparation were successful in demonstrating the mode conversion concept. We have shown, both in theory and experiment, an apparatus that has dual application: simultaneous nonseparable spin-orbit mode production, including controllable interdependence of polarization and spatial degrees of freedom, and HOM interference. Additionally we have made the two-input theory for the asymmetric Mach-Zehnder interferometer more concise and accessible and begun an investigation with the one-input case.

Overall, this study shows the ability to create a variety of controllable nonseparable spin-orbit modes of light from product modes while keeping open the possibility of HOM interference, using a simple asymmetric Mach Zehnder interferometer, and puts forward possibilities for their application.

Appendix A

Derivation of Identical Input Electric Field

The following describes the derivation of Eqn. 2.44: the electric field output function for an asymmetric Mach-Zehnder interferometer given two identical inputs. As stated in Section 2.1.7, the electric field is shown to be

$$\vec{\mathbf{E}}(\theta, \phi, \alpha, \beta; \delta; \rho, \Phi) = (\cos(\frac{\delta}{2}) \pm \sin(\frac{\delta}{2})) [\Psi_{\mp}(\theta, \phi, \alpha, \beta; \rho, \Phi)], \quad (\text{A-1})$$

where

$$\Psi_{\mp}(\theta, \phi, \alpha, \beta; \rho, \Phi) \equiv \cos(\frac{\alpha}{2}) \tilde{\mathbf{S}}_{\mp} \hat{\mathbf{y}} \mp i \sin(\frac{\alpha}{2}) e^{i\beta} \tilde{\mathbf{S}}_{\pm} \hat{\mathbf{x}}, \quad (\text{A-2})$$

and

$$\begin{aligned} \tilde{\mathbf{S}}_{\pm} &\equiv G(\rho) [\cos(\frac{\theta}{2}) \sin \Phi \pm i \sin(\frac{\theta}{2}) \cos \Phi e^{i\phi}], \\ \tilde{\mathbf{S}}_{\mp} &\equiv G(\rho) [\cos(\frac{\theta}{2}) \sin \Phi \mp i \sin(\frac{\theta}{2}) \cos \Phi e^{i\phi}]. \end{aligned} \quad (\text{A-3})$$

Then we can put all three parts together to find that

$$\begin{aligned} \vec{\mathbf{E}}(\theta, \phi, \alpha, \beta; \delta; \rho, \Phi) &= (\cos(\frac{\delta}{2}) \pm \sin(\frac{\delta}{2})) G(\rho) \times \\ &\quad \left[\cos(\frac{\alpha}{2}) (\cos(\frac{\theta}{2}) \sin \Phi \mp i \sin(\frac{\theta}{2}) \cos \Phi e^{i\phi}) \hat{\mathbf{y}} \right. \\ &\quad \left. \mp i \sin(\frac{\alpha}{2}) e^{i\beta} (\cos(\frac{\theta}{2}) \sin \Phi \pm i \sin(\frac{\theta}{2}) \cos \Phi e^{i\phi}) \hat{\mathbf{x}} \right]. \end{aligned} \quad (\text{A-4})$$

To make this equation compact, we can instead define the electric field as

$$\vec{\mathbf{E}}(\theta, \phi, \alpha, \beta; \delta; \rho, \Phi) = (\cos(\frac{\delta}{2}) \pm \sin(\frac{\delta}{2})) G(\rho) \times \left[\cos(\frac{\alpha}{2}) (R_{\mp} + iM_{\mp}) \hat{\mathbf{y}} \mp i \sin(\frac{\alpha}{2}) e^{i\beta} (R_{\pm} + iM_{\pm}) \hat{\mathbf{x}} \right], \quad (\text{A-5})$$

where

$$\begin{aligned} R_{\pm} &\equiv \text{Re}\{\tilde{\mathbf{S}}_{\pm}\} = \cos(\frac{\theta}{2}) \sin \Phi \mp \sin(\frac{\theta}{2}) \cos \Phi \sin \phi, \\ M_{\pm} &\equiv \text{Im}\{\tilde{\mathbf{S}}_{\pm}\} = \pm \sin(\frac{\theta}{2}) \cos \Phi \cos \phi, \\ R_{\mp} &\equiv \text{Re}\{\tilde{\mathbf{S}}_{\mp}\} = \cos(\frac{\theta}{2}) \sin \Phi \pm \sin(\frac{\theta}{2}) \cos \Phi \sin \phi, \\ M_{\mp} &\equiv \text{Im}\{\tilde{\mathbf{S}}_{\mp}\} = \mp \sin(\frac{\theta}{2}) \cos \Phi \cos \phi. \end{aligned}$$

The next step of the process is changing the format of each polarization coefficient from the current $R + iM$ form to a more intuitive $re^{i\gamma}$ form, which lends itself more easily to interpretation because both the amplitude and phase are stated plainly. The electric field can then be stated as

$$\begin{aligned} \vec{\mathbf{E}}(\theta, \phi, \alpha, \beta; \delta; \rho, \Phi) &= (\cos(\frac{\delta}{2}) \pm \sin(\frac{\delta}{2})) G(\rho) \times \\ &\left[\cos(\frac{\alpha}{2}) \sqrt{R_{\mp}^2 + M_{\mp}^2} \exp \left[i \tan^{-1} \left(\frac{M_{\mp}}{R_{\mp}} \right) \right] \hat{\mathbf{y}} \right. \\ &\quad \left. \mp i \sin(\frac{\alpha}{2}) e^{i\beta} \sqrt{R_{\pm}^2 + M_{\pm}^2} \exp \left[i \tan^{-1} \left(\frac{M_{\pm}}{R_{\pm}} \right) \right] \hat{\mathbf{x}} \right]. \quad (\text{A-6}) \end{aligned}$$

Next we remove the phase from the $\hat{\mathbf{y}}$ component, making it a global phase that will not effect the pattern of the output modes, and lumping together all phase factors that effect the pattern of the modes into the $\hat{\mathbf{x}}$ component. This leads to

$$\begin{aligned} \vec{\mathbf{E}}(\theta, \phi, \alpha, \beta; \delta; \rho, \Phi) &= (\cos(\frac{\delta}{2}) \pm \sin(\frac{\delta}{2})) G(\rho) \exp \left[i \tan^{-1} \left(\frac{M_{\mp}}{R_{\mp}} \right) \right] \times \\ &\left[\cos(\frac{\alpha}{2}) \sqrt{R_{\mp}^2 + M_{\mp}^2} \hat{\mathbf{y}} \right. \\ &\quad \left. \mp i \sin(\frac{\alpha}{2}) e^{i\beta} \sqrt{R_{\pm}^2 + M_{\pm}^2} \exp \left[i \left(\tan^{-1} \left(\frac{M_{\pm}}{R_{\pm}} \right) - \tan^{-1} \left(\frac{M_{\mp}}{R_{\mp}} \right) \right) \right] \hat{\mathbf{x}} \right]. \quad (\text{A-7}) \end{aligned}$$

Using the arctangent identity $\tan^{-1}(u) + \tan^{-1}(v) = \tan^{-1}(\frac{u+v}{1-uv})$ and the property of arctangent, $\tan^{-1}(-x) = -\tan^{-1}(x)$, the electric field can be condensed into

$$\begin{aligned} \vec{\mathbf{E}}(\theta, \phi, \alpha, \beta; \delta; \rho, \Phi) &= (\cos(\frac{\delta}{2}) \pm \sin(\frac{\delta}{2})) G(\rho) \exp \left[i \tan^{-1} \left(\frac{M_{\mp}}{R_{\mp}} \right) \right] \times \\ &\left[\cos(\frac{\alpha}{2}) \sqrt{R_{\mp}^2 + M_{\mp}^2} \hat{\mathbf{y}} \mp i \sin(\frac{\alpha}{2}) \sqrt{R_{\pm}^2 + M_{\pm}^2} \exp \left[i \left(\beta - \tan^{-1} \left(\frac{R_{\pm} M_{\mp} - R_{\mp} M_{\pm}}{R_{\pm} R_{\mp} + M_{\pm} M_{\mp}} \right) \right) \right] \hat{\mathbf{x}} \right]. \quad (\text{A-8}) \end{aligned}$$

The final step in the process is to call on the definitions of R_{\pm} , M_{\pm} , R_{\mp} , and M_{\mp} to solve for the arguments of the square roots in the vector amplitudes and the arctangent argument. This reduces the electric field function to

$$\begin{aligned} \vec{\mathbf{E}}(\theta, \phi, \alpha, \beta; \delta; \rho, \Phi) &= G(\rho) e^{\left[i \tan^{-1} \left(\frac{M_{\mp}}{R_{\mp}} \right) \right]} (\cos(\frac{\delta}{2}) \pm \sin(\frac{\delta}{2})) \\ &\left[\cos(\frac{\alpha}{2}) \sqrt{A_{+} \pm B \sin \phi} \hat{\mathbf{y}} \mp i \sin(\frac{\alpha}{2}) \sqrt{A_{+} \mp B \sin \phi} e^{\left[i \left[\beta \mp \tan^{-1} \left(\frac{B \cos \phi}{A_{-}} \right) \right] \right]} \hat{\mathbf{x}} \right], \quad (\text{A-9}) \end{aligned}$$

where

$$\begin{aligned} A_{\pm} &\equiv \cos^2(\frac{\theta}{2}) \sin^2 \Phi \pm \sin^2(\frac{\theta}{2}) \cos^2 \Phi, \\ B &\equiv \frac{1}{2} \sin \theta \sin(2\Phi), \end{aligned} \quad (\text{A-10})$$

as defined in Section 2.1.7.

Bibliography

- [1] Alan Isaacs, editor. *Oxford Dictionary of Physics*. Oxford University Press, 4 edition.
- [2] Albert Einstein. Concerning an Heuristic Point of View Toward the Emission and Transformation of Light. *Annalen der Physik*, 17:132–148, 1905.
- [3] Sonja Franke-Arnold and Aidan S. Arnold. Twisting Light to Trap Atoms: Photons carry a type of angular momentum that can guide, trap and rotate ultracold atoms and particles. *American Scientist*, 96(3):226–233, 2008.
- [4] A. Ashkin, J. M. Dziedzic, and T. Yamane. Optical trapping and manipulation of single cells using infrared laser beams. *Nature*, 330(6150):769–771, December 1987.
- [5] Ivan I. Smalyukh, Aliaksandr V. Kachynski, Andrey N. Kuzmin, and Paras N. Prasad. Laser Trapping in Anisotropic Fluids and Polarization-Controlled Particle Dynamics. *Proceedings of the National Academy of Sciences of the United States of America*, 103(48):18048–18053, 2006.
- [6] David J. Griffiths. *Introduction to Electrodynamics*. Addison-Wesley, 4 edition, October 2012.
- [7] B. M. Rodriguez-Lara and I. Ricardez-Vargas. Interference with polarized light beams: Generation of spatially varying polarization. *American Journal of Physics*, 77(12):1135–1143, December 2009.
- [8] Ryszard Horodecki, Pawel Horodecki, Michal Horodecki, and Karol Horodecki. Quantum entanglement. *Reviews of Modern Physics*, 81(2):865–942, June 2009.
- [9] D. Gottesman and I. L. Chuang. Demonstrating the viability of universal quantum computation using teleportation and single-qubit operations. *Nature*, 402(6760):390–393, November 1999.
- [10] E. Knill, R. Laflamme, and G. J. Milburn. A scheme for efficient quantum computation with linear optics. *Nature*, 409(6816):46–52, January 2001.
- [11] L. M. Duan, M. D. Lukin, J. I. Cirac, and P. Zoller. Long-distance quantum communication with atomic ensembles and linear optics. *Nature*, 414(6862):413–418, November 2001.
- [12] C. A. Muschik, I. de Vega, D. Porras, and J. I. Cirac. Quantum processing photonic states in optical lattices. *Physical Review Letters*, 100(6):063601–1–4, February 2008.

- [13] Christina E. Vollmer, Daniela Schulze, Tobias Eberle, Vitus Hndchen, Jaromr Fiurek, and Roman Schnabel. Experimental Entanglement Distribution by Separable States. *Physical Review Letters*, 111(23):230505, December 2013.
- [14] Stephan Ritter, Christian Nlleke, Carolin Hahn, Andreas Reiserer, Andreas Neuzner, Manuel Uphoff, Martin Mcke, Eden Figueroa, Joerg Bochmann, and Gerhard Rempe. An elementary quantum network of single atoms in optical cavities. *Nature*, 484(7393):195–200, April 2012.
- [15] Nicolas Sangouard, Christoph Simon, Hugues de Riedmatten, and Nicolas Gisin. Quantum repeaters based on atomic ensembles and linear optics. *Reviews of Modern Physics*, 83(1):33–80, March 2011.
- [16] Hong, Ou, and Mandel. Phys. Rev. Lett. 59, 2044 (1987) - Measurement of subpicosecond time intervals between two photons by interference.
- [17] Deepika Sundarraman. *The Manipulation of Transverse Spatial Mode and Polarization Degrees of Freedom of Light in an Asymmetric Interferometric System*. The College of Wooster, Wooster, OH, 2014.
- [18] Cody C. Leary, Maggie Lankford, and Deepika Sundarraman. Coupling of spin and orbital degrees of freedom in tunable Hong-Ou-Mandel interference involving photons in hybrid spin-orbit modes. In *SPIE Optics+ Optoelectronics*, pages 95050T–95050T. International Society for Optics and Photonics, 2015.
- [19] Cody Collin Leary. *Measurement and Control of Transverse Photonic Degrees of Freedom via Parity Sorting and Spin-Orbit Interaction*. PhD thesis, University of Oregon, June 2010.
- [20] A. E. Siegman. *Lasers*. University Science Books, January 1986.
- [21] George B. Arfken and Hans-Jurgen Weber. *Mathematical methods for physicists*. Academic Press, San Diego, 4th ed edition, 1995.
- [22] Hermite Polynomial. <http://mathworld.wolfram.com/HermitePolynomial.html>, 2016.
- [23] Mounted Zero-Order Half-Wave Plates. https://www.thorlabs.com/newgrouppage9.cfm?objectgroup_id=711, 2016. [online; accessed 2016, February].
- [24] Margaret E. Raabe. *Manipulation of a Photon’s Spatial Wave Function in Optical Fibers*. The College of Wooster, Wooster, OH, 2012.
- [25] Ivan Moreno, Gonzalo Paez, and Marija Strojnik. Dove Prism with Increased Throughput for Implementation in a Rotational-Shearing Interferometer. *Applied Optics*, 42(22):4514, 2003.
- [26] Leo Levi. *Applied optics; a guide to optical system design*. Wiley series in pure and applied optics. Wiley, New York, 1968.
- [27] New Focus Tech Support. User’s Guide: The Berek Polarization Compensator, Model 5540, 2012.

- [28] Michael W. Davidson. Polarized Light Microscopy: The Berek Compensator, November 2015. Maintained by The Florida State University in collaboration with Optical Microscopy at the National High Magnetic Field Laboratory.
- [29] C. C. Leary, Maggie Lankford, and Deepika Sundarraman. Polarization-based control of spin-orbit vector modes of light in biphoton interference. *Optics Express*, 2016.
- [30] Rodney Loudon. *The Quantum Theory of Light*. Oxford University Press, 3 edition, November 2000.
- [31] R. Clark Jones. A New Calculus for the Treatment of Optical Systems. *Journal of the Optical Society of America*, 31(7):488, July 1941.
- [32] A. Gerrard and J. M. Burch. *Introduction to matrix methods in optics*. Wiley series in pure and applied optics. Wiley, London, New York, 1975.
- [33] Brahim Lounis and Michel Orrit. Single-photon sources. *Reports on Progress in Physics*, 68(5):1129–1179, 2005.
- [34] Cody C. Leary, Maggie Lankford, and Deepika Sundarraman. Investigating the role of distinguishability in two-photon mechanics in the undergraduate laboratory. *American Journal of Physics*, June 2015.
- [35] David J. Griffiths. *Introduction to quantum mechanics*. Prentice Hall, Englewood Cliffs, N.J, 1995.
- [36] Jared W. Haslett. Phase waves of louis debroglie. *American Journal of Physics*, 40(9), 1972.
- [37] Thomas F. Gilliss. *Manipulation of Transverse Photonic Degrees of Freedom Via Classical Hong-Ou-Mandel Interference*. The College of Wooster, Wooster, OH, 2013.
- [38] UV Fused Silica Broadband Plate Beamsplitters (Coating: 400 - 700 nm). https://www.thorlabs.com/newgrouppage9.cfm?objectgroup_id=4807&pn=BSW10, 2016. [online; accessed 2016, March 6].
- [39] J. Pan. Experimental manipulation of photons and cold atoms: towards scalable quantum information processing. Conference on Lasers and Electro-Optics/Pacific Rim, (Optical Society of America), January 2009.
- [40] D. Gonta and P. van Loock. Dynamical quantum repeater using cavity QED and optical coherent states. *Physical Review A (Atomic, Molecular, and Optical Physics)*, 88(5):052308, November 2013.
- [41] Harland G. Tompkins and Eugene A. Irene, editors. *Handbook of ellipsometry*. William Andrew Pub. ; Springer, Norwich, NY : Heidelberg, Germany, 2005.